Supercritical CH3OH-triggered isotype heterojunction and groups in g-C3N4 for enhanced photocatalytic H2 evolution

Liuhao Mao, Binjiang Zhai, Jinwen Shi, Xing Kang, Bingru Lu, Yanbing Liu, Cheng Cheng, Hui Jin, Eric Lichtfouse, Liejin Guo

ACS Nano 2024 https://doi.org/10.1021/acsnano.4c03922

Supercritical CH_3OH-Triggered Isotype Heterojunction and Groups in g-C_3N_4 for Enhanced Photocatalytic H_2Evolution

Liuhao Mao,[†] Binjiang Zhai,[†] Jinwen Shi,[*] Xing Kang, Bingru Lu, Yanbing Liu, Cheng Cheng, Hui Jin, Eric Lichtfouse, and Liejin Guo

ABSTRACT: **The structure tuning of bulk graphitic carbon nitride (g-C_3N_4) is a critical way to promote the charge carriers dynamics for enhancing photocatalytic H_2-evolution activity. Exploring feasible post-treatment strategies can lead to effective structure tuning, but it still remains a great challenge. Herein, a supercritical CH_3OH (ScMeOH) post-treatment strategy (250−300 °C, 8.1−11.8 MPa) is developed for the structure tuning of bulk g-C_3N_4. This strategy presented advantages of time-saving (less than 10 min), high yield (over 80%), and scalability due to the enhanced mass transfer and high reactivity of ScMeOH. During the ScMeOH post-treatment process, CH_3OH molecules diffused into the interlayers of g-C_3N_4 and subsequently participated in *N*-methylation and hydroxylation reactions with the intralayers, resulting in a partial phase transformation from g-C_3N_4 into carbon nitride with a poly(heptazine imide)-like structure (Q-PHI) as well as abundant methyl and hydroxyl groups. The modified g-C_3N_4 showed enhanced photocatalytic activity with an H_2-evolution rate 7.2 times that of pristine g-C_3N_4, which was attributed to the synergistic effects of the g-C_3N_4/Q-PHI isotype heterojunction construction, group modulation, and surface area increase. This work presents a post-treatment strategy for structure tuning of bulk g-C_3N_4 and serves as a case for the application of supercritical fluid technology in photocatalyst synthesis.**

KEYWORDS: *graphitic carbon nitride, hydrogen, poly(heptazine imide), supercritical methanol, solvothermal treatment*

The development of hydrogen (H_2) energy technology is instrumental in achieving the objective of carbon neutrality.[1] Among various H_2-production technologies, photocatalytic H_2 production from water is an effective, green, and promising route.[2,3] The performance of photocatalytic H_2 production hinges on the photocatalyst, and the structure tuning of the photocatalyst by post-treatment is a commonly used strategy to enhance the performance of the photocatalyst.[4] Comprehensive evaluation in various aspects including photocatalytic activity, stability, light-response range, toxicity, preparation difficulty, cost and so on is crucial in determining excellent photocatalysts.[5]

Graphitic carbon nitride (g-C_3N_4) emerges as a promising photocatalyst for H_2 evolution. First, it consists of earth-abundant nonmetallic elements and is usually synthesized by a facile thermal polymerization process using common precursors such as dicyandiamide, melamine, and urea, which makes it cheap and environmentally friendly. Additionally, it is responsive to visible light and exhibits good stability. However, the practical applications of g-C_3N_4 in photocatalytic H_2 production are still limited by the inadequate specific surface area and the severe recombination rate of the charge carrier.[6−8] To overcome these inherent deficiencies of bulk g-C_3N_4, structure tuning by post-treatment such as thermal treatment,[9] plasma treatment,[10] ionothermal treatment,[11,12] and hydrothermal/solvothermal treatment[13] have been developed. In addition to the photocatalytic performance of modified g-C_3N_4 after post-treatment, some issues such as yield, required time, equipment requirement, and operation process should also be considered for the modification strategy. Therefore, it is

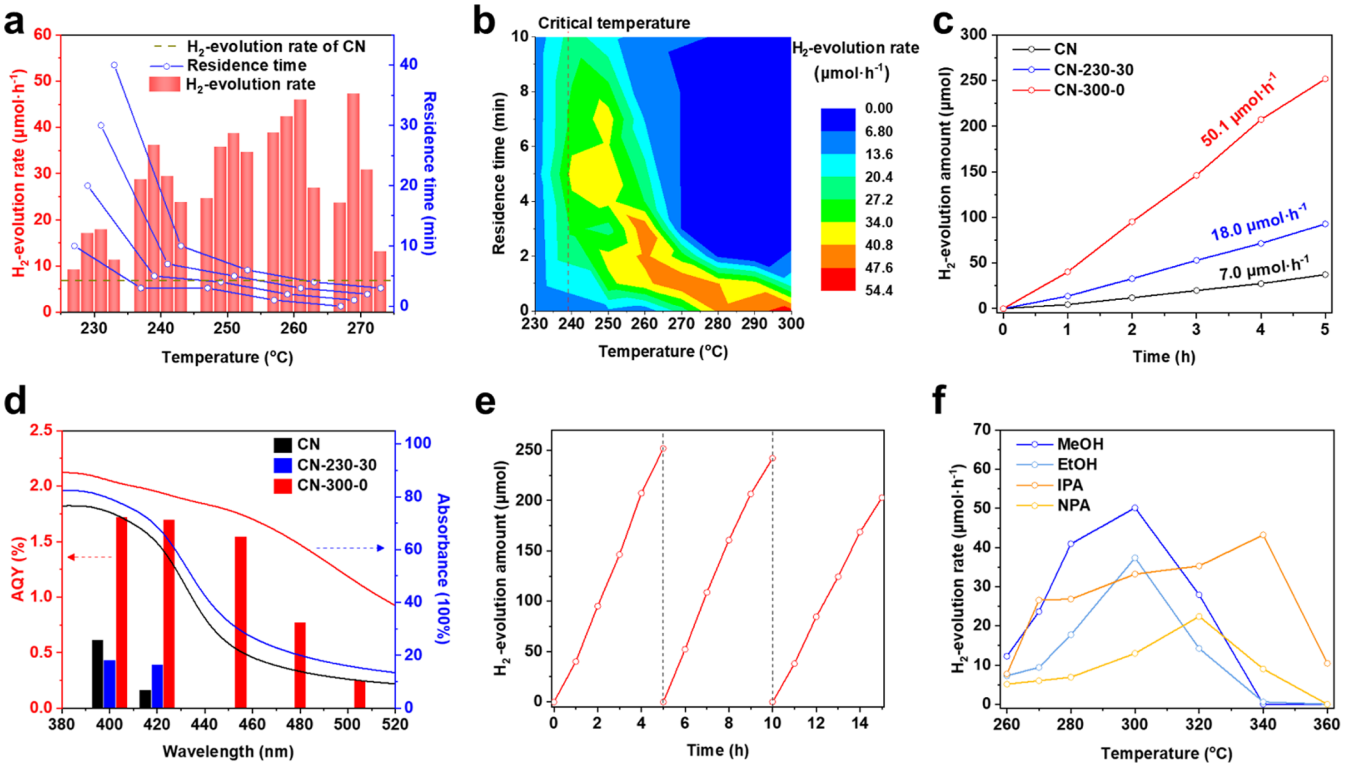

Figure 1. (a) Photocatalytic H_2-evolution rates (left axis) of CN-*T*-*t* samples by different post-treatment temperatures (horizontal axis) and the corresponding residence time (right axis). (b) Contour map between photocatalytic H_2-evolution rate, post-treatment temperature, and residence time. Panel (b) was plotted based on the data from Table S1. (c) Time courses and (d) action spectra of photocatalytic H_2 evolution for CN, CN-230-30, and CN-300-0. Left axis: wavelength-dependent AQYs; right axis: UV−vis absorbance. (e) Stability test of the photocatalytic H_2 evolution for CN-300-0. (f) Photocatalytic H_2-evolution rates of modified g-C_3N_4 by different alcohols (MeOH, EtOH, IPA, and NPA) post-treatment with a residence time of 0 min at different post-treatment temperatures.

meaningful to develop an approach for g-C_3N_4 modification with the benefits of being effective, green, high-yielding, and scalable.

Supercritical fluids (SCFs) display unique physicochemical properties such as low viscosity, zero surface tension, and high diffusivity.[14] The SCF technology has received much attention in the fields of nanomaterial synthesis ranging from scientific research to industrial application.[15−19] Owing to the solvation behavior and enhanced mass transfer ability of SCFs, a homogeneous reaction environment could be formed by dissolving chemicals (including metal precursor, organic solvent, surfactant, redox agent, and so on) in SCFs, realizing a rapid SCF-assisted hydrothermal/solvothermal synthesis of metals, metal hydroxides, metal oxides, metal sulfides, metal−organic frameworks, and composites.[20−22] On the other hand, structure tuning of nanomaterials such as exfoliation,[23−26] surface reduction and oxidation,[27] phase engineering,[28−30] and elemental doping[31−33] could be realized by the post-treatment strategy utilizing SCFs. Among numerous SCFs, supercritical H_2O (ScH_2O) and supercritical CO_2 ($ScCO_2$) are extensively employed in the preparation and modification of nanomaterials.[34,35] Recently, supercritical alcohols have become another important SCF following ScH_2O and $ScCO_2$.[36] Supercritical alcohols represented by supercritical CH_3OH (ScMeOH) have been used to synthesize various functional nanomaterials. For instance, reduced graphene oxide[37,38] and TiO_2−graphene composite[39] have been prepared using supercritical alcohols. Anthracite coal has been converted into ribbon-like graphitic materials using supercritical ethanol with a yield of 6.4 wt %.[40] The critical condition of ScMeOH (239.4 °C, 8.1 MPa) is more moderate than that of ScH_2O (374.1 °C, 22.1 MPa), while its critical pressure is approximate to that of $ScCO_2$ (7.4 MPa). Additionally, the low boiling point of CH_3OH (64.7 °C) facilitates its separation from the product. Compared with conventional CH_3OH, ScMeOH has lower hydrogen bonding, dielectric coefficient, surface tension, and viscosity and a much higher diffusion coefficient, rendering ScMeOH as an excellent reaction medium. ScMeOH is also electronegative and nucleophilic, thus allowing reactions such as alkylation, alcoholysis, and polymer degradation.[41,42] In addition, ScMeOH decomposition produces a reductive medium containing H_2 and CO and hydroxyl ions.[43]

In our previous attempt, it was found that g-C_3N_4 decomposed completely by the ScH_2O post-treatment due to excessive oxidation of ScH_2O.[44] Herein, a ScMeOH post-treatment strategy was proposed for structure tuning of g-C_3N_4, and the optimal post-treatment conditions as well as the critical role of the supercritical state of MeOH for g-C_3N_4 modification were explored. Through detailed characterizations of modified g-C_3N_4 and analysis of liquid/gas products after the ScMeOH post-treatment, the structural evolution of g-C_3N_4 and the mechanism of enhanced photocatalytic H_2-evolution activity for modified g-C_3N_4 were also investigated.

RESULTS AND DISCUSSION

Evaluation of the Photocatalytic H_2-Evolution Performance. In this study, a series of modified g-C_3N_4 (CN-*T*-*t*, where *T* was the post-treatment temperature and *t* was the residence time at the target post-treatment temperature) were

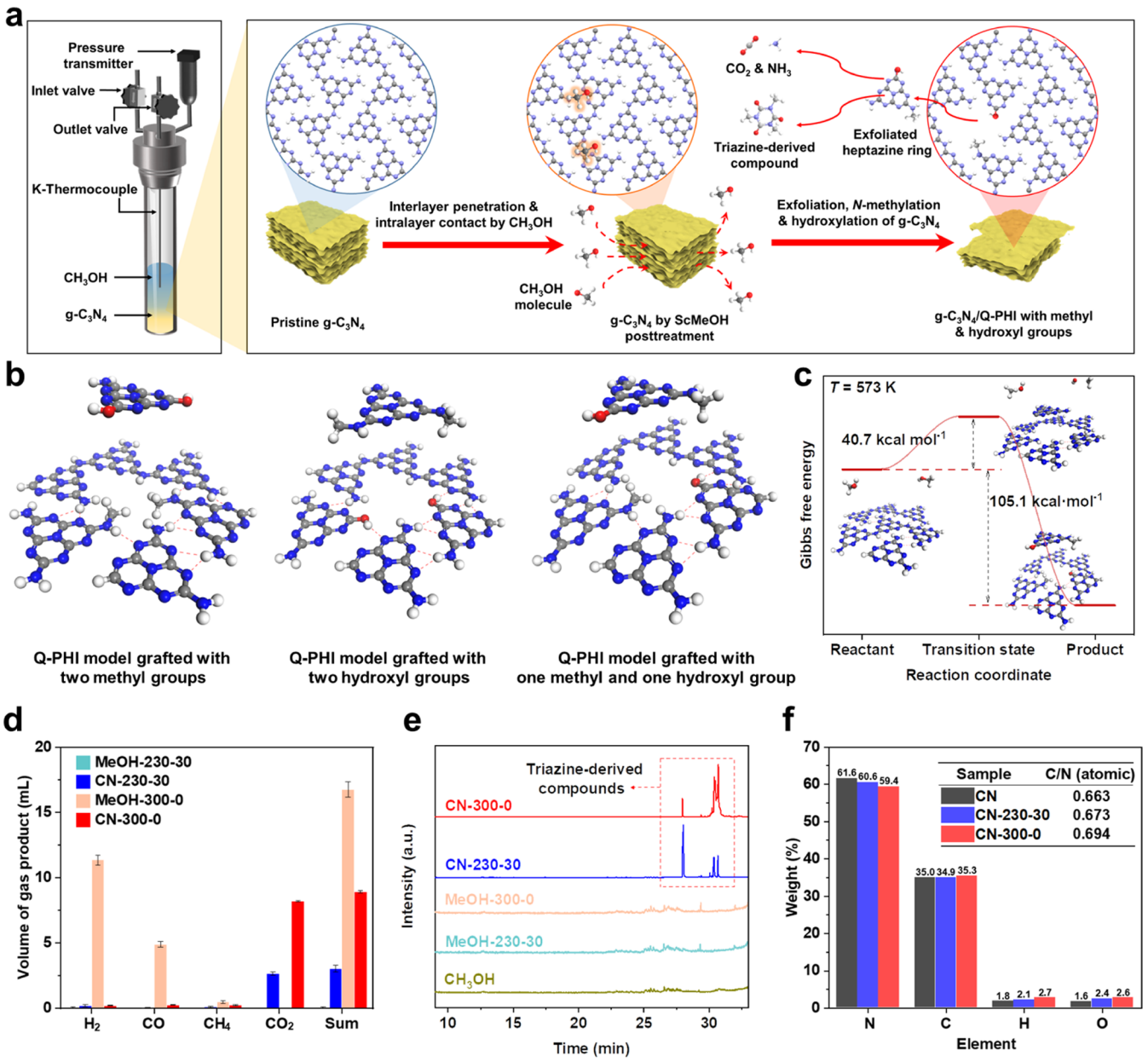

Figure 2. (a) Schematic illustration of the structural evolution of g-C_3N_4 by the ScMeOH post-treatment. (b) Three kinds of Q-PHI models with different groups and the corresponding exfoliated units. (c) Gibbs free energies calculated by molecular dynamics simulations for the formation pathways of Q-PHI with one methyl and one hydroxyl group. (d) Composition analysis of gas products from MeOH-230-30, CN-230-30, MeOH-300-0, and CN-300-0. (e) Composition analysis of CH_3OH and the liquid products from MeOH-230-30, CN-230-30, MeOH-300-0, and CN-300-0. MeOH-230-30 and MeOH-300-0 were blank runs in the absence of g-C_3N_4. (f) Element contents for CN, CN-230-30, and CN-300-0.

prepared by the solvothermal post-treatment of g-C_3N_4 in subcritical or supercritical CH_3OH. Throughout the post-treatment process, temperature and pressure data were continuously recorded in real-time, as shown in Figure S1. The photocatalytic H_2-evolution activities of modified g-C_3N_4 are shown in Figure 1a,b. As for the modified g-C_3N_4 by subcritical CH_3OH (SubMeOH) post-treatment at 230 °C for 10−40 min, the optimal sample CN-230-30 showed a photocatalytic H_2-evolution rate of 18.0 μmol·h^{-1}. Interestingly, when the post-treatment temperature exceeded the critical point of CH_3OH (239.4 °C), the photocatalytic H_2-evolution activities of modified g-C_3N_4 by the ScMeOH post-treatment underwent a sudden enhancement compared with the modified g-C_3N_4 by the SubMeOH post-treatment, simultaneously the corresponding required residence time decreased sharply from tens of minutes to a few minutes. The apparent colors of modified g-C_3N_4 could also be reflected by reactivity differences between SubMeOH and ScMeOH post-treatments, and the result is shown in Figure S2. The apparent colors of modified g-C_3N_4 by the SubMeOH post-treatment (CN-230-*x*, *x* = 5, 10, 20, 30, 40) were light yellow, similar to CN, and the structure of modified g-C_3N_4 by the ScMeOH post-treatment (such as CN-270-5, CN-280-3, and CN-290-2) was susceptible to damage and manifested as blackening with increased post-treatment temperature and residence time. It was found that ScMeOH was more effective and efficient for g-

C_3N_4 modification compared with SubMeOH, and the high reactivity of ScMeOH determined that the residence time was very crucial and sensitive for g-C_3N_4 modification.

Three typical samples were selected for further analysis, including a sample of pristine g-C_3N_4 (CN), a modified g-C_3N_4 by prolonged the SubMeOH post-treatment (CN-230-30) and a modified g-C_3N_4 by a rapid ScMeOH post-treatment (CN-300-0). As shown in Figure 1c,d, CN-300-0 showed the best photocatalytic H_2-evolution rate of 50.1 μmol·h^{-1}, which was 2.8 times that of CN-230-30 and 7.2 times that of CN, and it showed obvious higher apparent quantum yield (AQY) values as expected based on the photocatalytic H_2-evolution activity. Specifically, CN-300-0 showed a certain AQY values of 1.55% (450 nm), 0.78% (475 nm), and 0.25% (500 nm), while the AQY values of CN and CN-230-30 were not detected at the wavelength higher than 450 nm, and these results were in agreement with the UV−vis spectra. In addition, Figure 1e presents the cyclic photocatalytic H_2-evolution test for CN-300-0, and there was little decay after three cyclic tests (15 h), indicating good photocatalytic stability of the modified g-C_3N_4 by the ScMeOH post-treatment. It was worth mentioning that g-C_3N_4 was not only modified by the ScMeOH post-treatment effectively and efficiently compared with conventional solvothermal post-treatment (Table S2) but also exhibited an advantage of high yield, and the yield of CN-300-0 could reach 80.1% with the initial dispersion concentration as 100 mg·mL^{-1} (Figure S3). Moreover, when g-C_3N_4 was modified by the SCF post-treatment using other alcohols including ethanol (EtOH), 1-propanol (NPA), and isopropanol (IPA), the photocatalytic activities of modified g-C_3N_4 could also be improved (Figure 1f).

Structure Tuning of g-C_3N_4 by the ScMeOH Post-Treatment. Ideal g-C_3N_4 is composed of few-layer 2D nanosheets bonded by van der Waals forces, and the in-plane structure of the nanosheet is composed of repeating units of continuous heptazine (Figure S4a). However, pristine g-C_3N_4 prepared from the thermal condensation of melamine is usually amorphous (Figure S4b).[45] In this work, structure tuning of g-C_3N_4 was realized by a ScMeOH post-treatment strategy, as depicted in Figure 2a. In this process, the CH_3OH molecules in the supercritical state diffused into the interlayers of g-C_3N_4 and contacted with the intralayers. The high reactivity of ScMeOH further led to breakages of C−N bonds between NH-bridged melem monomers, and the amino group was expected to be electrophilically attacked by the methyl group, while the heptazine ring was expected to be nucleophilically attacked by the hydroxyl group, resulting in *N*-methylation and hydroxylation reactions, respectively (Figure S5). The ordered breakage of C−N bridging bonds led to the regular knocking out of heptazine rings from melon polymer; simultaneously, *N*-methylation and hydroxylation reactions occurred in the intralayers of g-C_3N_4, forming a carbon nitride with a poly(heptazine imide) (PHI)-like structure as well as abundant methyl and hydroxyl groups. In general, PHI refers to the structure with high crystallinity, which is typically synthesized by the ionthermal treatment of melon polymers,[46] thereby the PHI-like structure transformed from amorphous g-C_3N_4 in this work was termed as quasi-poly(heptazine imide) (Q-PHI). Figure S6 displays the basic structure unit of PHI and Q-PHI. According to the substitution positions of methyl and hydroxyl groups, there were three kinds of potential Q-PHI models, as shown in Figure 2b, and the corresponding chemical formulas of exfoliated units are listed in Table S2. In addition, theoretical calculations were conducted to analyze the feasibility of the reactions, and the result is shown in Figure 2c. Specifically, the Gibbs free energy pathways for *N*-methylation and hydroxylation reactions in g-C_3N_4 were analyzed. The reaction of Q-PHI formation was spontaneous in thermodynamics due to the negative value of the Gibbs free energy change (ΔG = −105.1 kcal·mol^{-1}). In addition, more CH_3OH molecules enabled to overcome the energy barrier (40.7 kcal·mol^{-1}) at high temperature and pressure in chemical kinetics, which was in good accordance with the experimental results that the Q-PHI formation reaction occurred spontaneously and quickly under high temperature and pressure.

Analysis of the gas and liquid products after solvothermal post-treatment and the corresponding blank runs (in the absence of g-C_3N_4) was conducive to understanding the structural evolution of g-C_3N_4 by the ScMeOH post-treatment. The temperature and pressure curves for the post-treatment process of CN-230-30, CN-300-0, and the corresponding blank runs are shown in Figure S7. The composition of gas products was detected by gas chromatography (GC), and the results are shown in Figures 2d and S8, and the volume of gas products was measured using a graduated syringe, as shown in Figure S9. There was almost no CH_3OH decomposition from MeOH-230-30, since only a trace of H_2 was detected, while certain amounts of H_2 (11.4 mL), CO (4.9 mL), and CH_4 (0.49 mL) were produced from MeOH-300-0. The proposed relevant reactions are provided in eqs 1 and 2.

$$CH_3OH \rightarrow CO + 2H_2 \quad (1)$$

$$CO + 3H_2 \rightarrow CH_4 + H_2O \quad (2)$$

It was found that neither MeOH-230-30 nor MeOH-300-0 had any detectable CO_2, while a significant amount of CO_2 was produced when g-C_3N_4 participated in the solvothermal reaction, simultaneously reducing gases (H_2, CO) almost disappeared, resulting in the gas products from CN-230-30 and CN-300-0 being mainly composed of CO_2. Specifically, the CO_2 amounts in the gas phase were 2.7 mL from CN-230-30 and 8.2 mL from CN-300-0, whose proportions were calculated as 88.0 and 91.8%, respectively. Furthermore, the composition of liquid products was measured by the combination of gas chromatography and mass spectrometry (GC−MS), and the results are shown in Figures 2e and S10. The GC−MS analysis of CH_3OH could be regarded as a baseline, and the GC−MS analysis of liquid products from MeOH-230-30 and MeOH-300-0 exhibited similarity with CH_3OH. In contrast, several significant peaks appeared in the GC−MS signals for the liquid products from CN-230−30 and CN-300-0, which were identified as a series of triazine-derived compounds utilizing mass spectrometry. The formation of these compounds resulted from the reaction between ScMeOH and the exfoliated heptazine rings, and the formed short-chain organic compounds were further transformed into CO_2 and NH_3 with the help of ScMeOH and reducing gases. It was also consistent with the result of the appearance of CO_2 and the disappearance of H_2 in the gas products from CN-230-30 and CN-300-0. Moreover, the preparation of CN-300-0 produced a greater amount of CO_2 in gas products and a higher concentration of triazine-derived compounds in liquid products than those of CN-230-30, indicating that ScMeOH was more effective and efficient for structure tuning of g-C_3N_4 than SubMeOH. Figure 2f shows the element contents for samples measured by an elemental analyzer. According to the

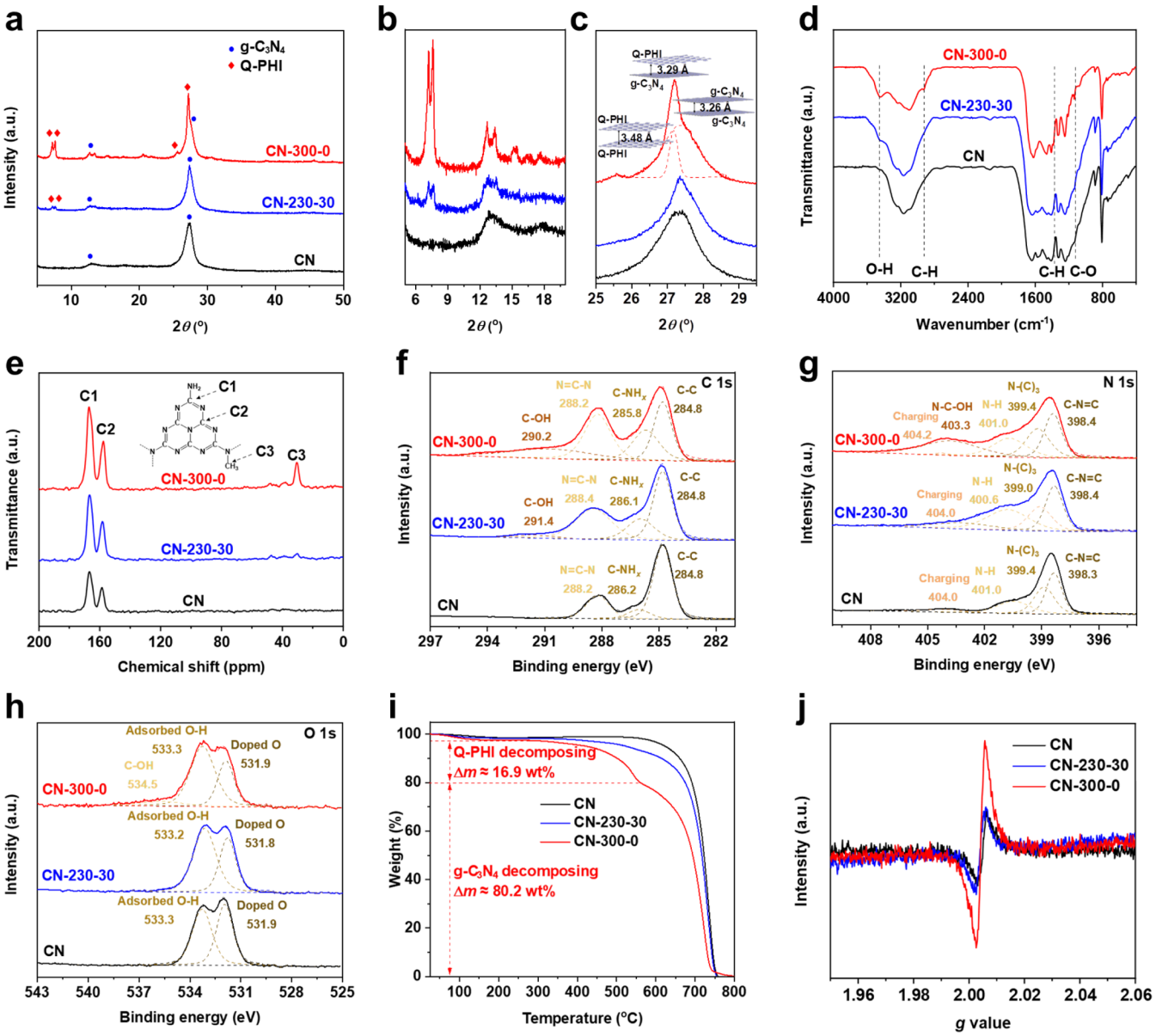

Figure 3. (a) XRD patterns, (b, c) partially magnified details of XRD patterns in (a), (d) FTIR spectra, (e) solid-state ^{13}C NMR spectra, (f–h) high-resolution XPS of (f) C 1s, (g) N 1s, and (h) O 1s orbitals, (i) TG curves, and (j) dark solid-state EPR spectra for CN, CN-230-30, and CN-300-0.

Q-PHI models with different grafted groups and the corresponding chemical formulas of exfoliated units in Table S3, the formation of Q-PHI and the grafting of methyl and hydroxyl groups comprehensively increased the C/N atomic ratio and also increased the H and O content in modified g-C_3N_4.

As shown in Figure 3a, two characteristic peaks at around 12.8 and 27.3°, which were attributed to (100) and (002) diffraction facets of g-C_3N_4, were found in CN, CN-230-30, and CN-300-0. Two new dominant characteristic diffraction peaks at 7.2 and 7.6°, which were ascribed to the (100) diffraction facet of the Q-PHI structure, appeared in both CN-230-30 and CN-300-0 (Figure 3b).[46] The in-planar arrangement of Q-PHI was asymmetric due to the introduction of methyl and hydroxylation groups, thus forming two independent X-ray diffraction (XRD) characteristic peaks of the Q-PHI phase. In addition, the overlapping (002) XRD peak in CN-300-0 could be deconvoluted into three XRD peaks located at 25.6, 27.1, and 27.3°, and the corresponding interlayer spacing values were 3.48, 3.29, and 3.26 Å, respectively (Figure 3c). The grafted methyl and hydroxyl groups in the Q-PHI component expanded the interlayer spacing;[47] consequently, the three different values mentioned above represented the interlayer spacings of Q-PHI/Q-PHI, g-C_3N_4/Q-PHI, and g-C_3N_4/g-C_3N_4, respectively. Interestingly, when other alcohols including EtOH, NPA, and IPA were employed as SCFs for the g-C_3N_4 post-treatment, there was no Q-PHI component in the optimally modified g-C_3N_4 according to the XRD patterns (Figure S11). It was deduced that the CH_3OH molecule was more matching to penetrate the interlayers of g-C_3N_4 than longer-chain alcohols due to its smaller molecular size. Additionally, the free energy barrier of reaction for Q-PHI formation caused by CH_3OH was lower compared to that of longer-chain alcohols such as C_2H_5OH

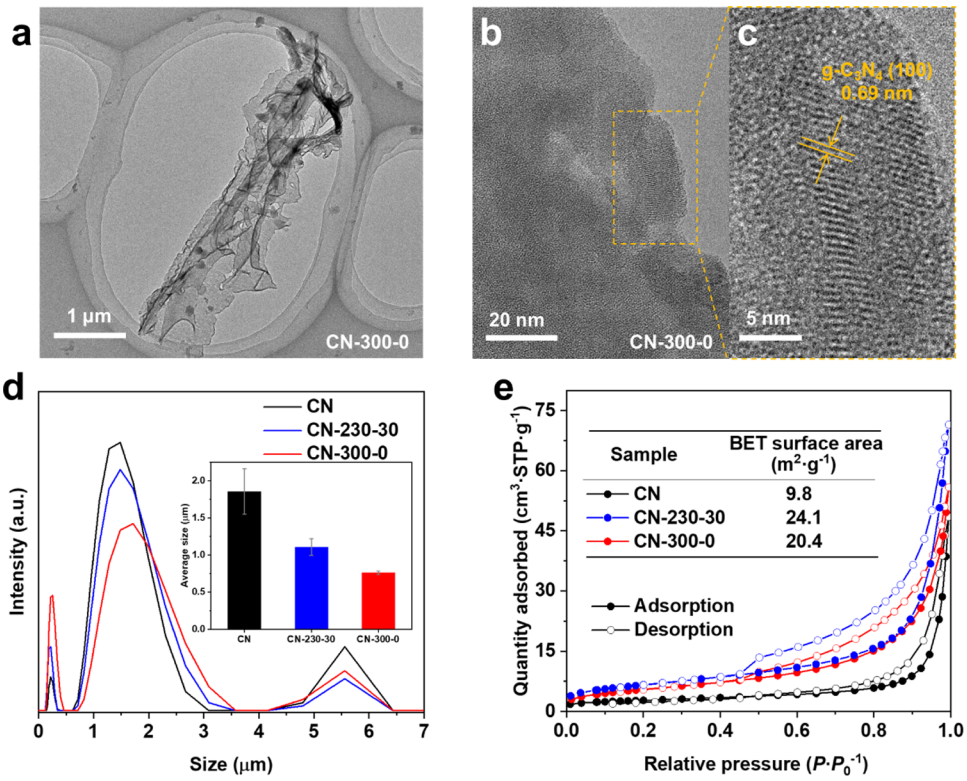

Figure 4. (a) TEM image, (b) high-resolution TEM image, and (c) magnified image of selected area in (b) for CN-300-0. Scale bar: (a) 1 μm, (b) 20 nm, and (c) 5 nm. (d) Dynamic light scattering spectra and (inset) the average sizes and (e) N_2 adsorption−desorption isotherms for CN, CN-230-30, and CN-300-0.

(Figure S12). Taking IPA-340-0 as an example, the main structure tuning occurred on the surface of g-C_3N_4 through supercritical IPA post-treatment, leading to abundant isopropyl groups being grafted onto the surface of g-C_3N_4. The modification of the surface isopropyl groups contributed to the enhanced photocatalytic activity, as shown in Figure 1f.

Fourier transform infrared (FTIR) spectra were recorded to investigate the molecular structure and chemical bonds in the samples. As shown in Figure 3d, for all three samples, a sequence of representative absorption peaks that were attributed to the bending or stretching vibration modes of C−N heterocyclic rings was found at 1641, 1571, 1410, 1321, and 1241 cm^{-1}, and the peak at 807 cm^{-1} was identified as the breathing modes of s-triazine ring units. On account of both g-C_3N_4 and Q-PHI being composed of heptazine rings, CN, CN-230-30, and CN-300-0 exhibited similar FTIR patterns at the above-mentioned positions. Furthermore, CN-230-30 and CN-300-0 displayed a broad band in the range 3350−3650 cm^{-1}, which was attributed to the mode of vibration of hydroxyl groups. Distinct peaks including a peak at 2930 cm^{-1}, corresponding to the stretching mode of C−H, a peak at 1386 cm^{-1}, corresponding to the bending mode of C−H, and a peak at 1135 cm^{-1}, corresponding to the stretching mode of C−O, were observed in CN-300-0. The variations of peaks that were attributed to the O−H, C−H, and C−O bonds indicated the appearance of more hydroxyl and methyl groups in the modified g-C_3N_4 by the ScMeOH post-treatment. Furthermore, Figure 3e shows the solid-state ^{13}C nuclear magnetic resonance (NMR) spectra of CN, CN-230-30, and CN-300-0 that could reveal the chemical state of C atoms. Two strong peaks at 167.1 and 157.7 ppm were observed for all samples, which could be attributed to the N_2−C−NH_x (C1 atoms) and C−N_3 (C2 atoms) in the tri-s-triazine ring, respectively.[48] Another new peak with a chemical shift of approximately 30.4 ppm appeared in the ^{13}C NMR spectrum of CN-300-0, and a weak peak was observed at the same location in the spectrum of CN-230-30. It could be ascribed to the methyl groups grafted into the Q-PHI skeleton.[49]

X-ray photoelectron spectra (XPS) were measured to investigate more structural information, and the results are shown in Figure 3f−h and Table S4. The C 1s XPS of CN could be fitted into three peaks indexed to standard carbon (284.8 eV), sp^2-hybridized C in C−NH_x (286.0 eV), and sp^2-hybridized C in N−C═N (288.2 eV). The N 1s XPS of CN could be fitted into four peaks indexed to sp^2-hybridized N in C−N═C (398.4 eV), sp^3-hybridized in N−$(C)_3$ (398.9 eV), amino functions (400.5 eV), and charging effect (404.0 eV). The C 1s and N 1s XPS of CN-230-30 and CN-300-0 could also be fitted in a similar fitting rule. Compared with CN, another C 1s peak appeared in CN-230-30 (291.4 eV) and CN-300-0 (290.2 eV), which could be ascribed to sp^2-hybridization in C−OH, and a new N 1s peak appeared in CN-300-0 (403.3 eV), which could be ascribed to N species in N−C−OH. The binding energies of C 1s in N═C−N and N 1s in C═N−C for all samples were positioned at similar locations without a significant shift, since the basic heptazine heterocyclic rings of modified g-C_3N_4 were not destroyed. Moreover, the C 1s peak of C−N for CN-300-0 (285.7 eV) shifted to lower binding energy in comparison with those for CN (286.0 eV) and CN-230-30 (286.0 eV), while the N 1s peak of N−$(C)_3$ for CN-300-0 (399.2 eV) shifted to higher binding energy in comparison with those for CN (398.9 eV) and CN-230-30 (399.1 eV). It should be attributed to the breaking of bridge linkages in heptazine rings, leading to the

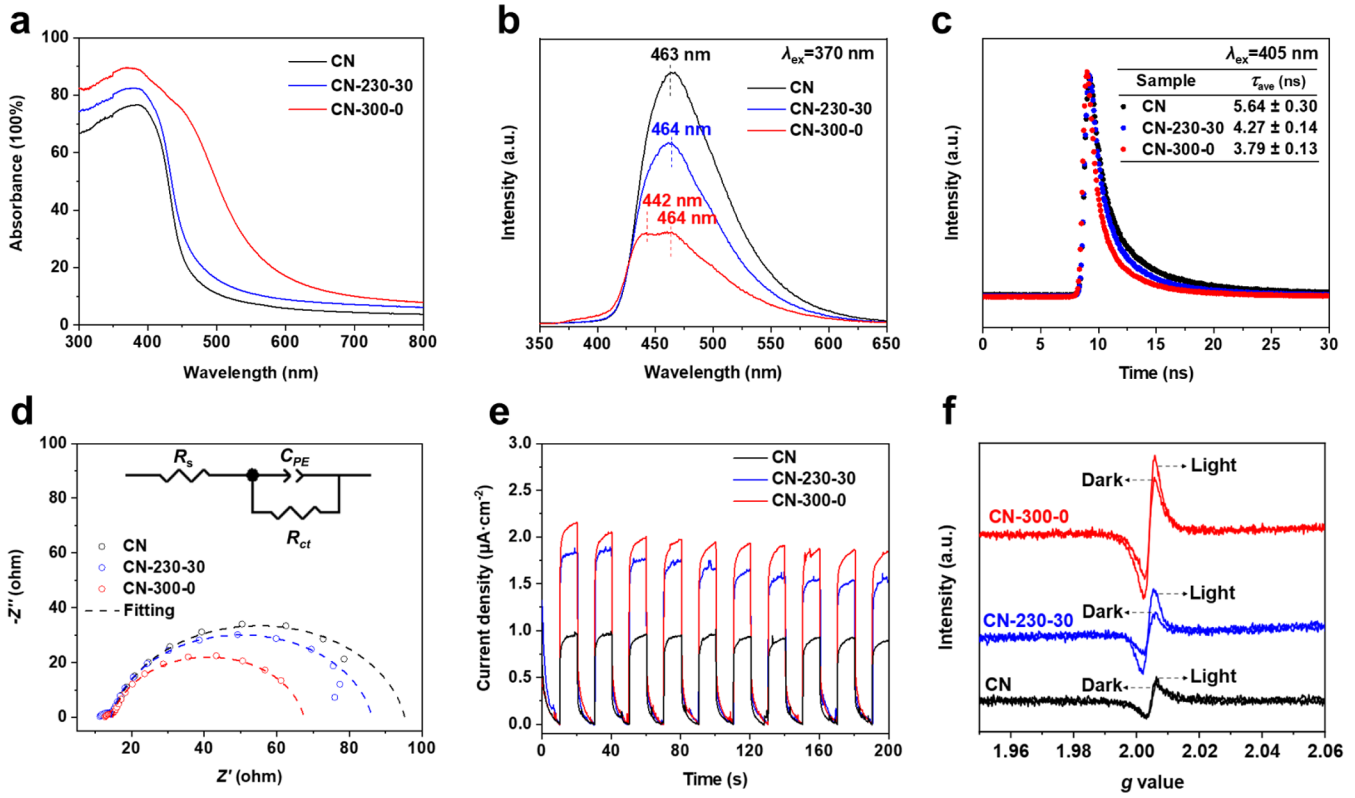

Figure 5. (a) UV−vis spectra, (b) steady-state PL spectra, (c) time-resolved PL decay spectra, (d) EIS results, (e) transient photocurrent curves under chopped light irradiation, and (f) solid-state EPR spectra for CN, CN-230-30, and CN-300-0 in the dark and under light irradiation. The inset in (d) shows an equivalent circuit. R_s: electrolyte resistance; R_{ct}: charge-transfer resistance from the electrode to the electrolyte; and C_{PE}: constant phase element.

surrounding chemical environment change. In addition, the O 1s spectrum of CN was fitted into two peaks belonging to the surface-adsorbed hydroxyl group (531.9 eV) and doped O (533.3 eV). Another O 1s XPS peak of the grafted hydroxyl (534.5 eV) was detected in CN-300-0. In addition, the survey-scan XPS of all samples as well as the Ni 2p and Cr 2p high-resolution XPS of CN-300-0 (Figure S13). There was no XPS signal attributed to metallic elements (including Ni, Cr, and Mo) detected in CN-300-0, thereby excluding the impacts of detached alloy particles in this study.

The thermogravimetric (TG) curves of the samples are shown in Figure 3i. CN remained stable up to 570 °C and decomposed completely up to 750 °C, and the TG curve of CN-230-30 revealed the analogous characteristics as CN. Different from CN and CN-230-30, CN-300-0 exhibited two significant decomposition stages. The first stage from 350 to 550 °C represented the decomposition of the Q-PHI component (~16.9%,) and the second stage from 550 to 750 °C corresponded to the decomposition of the g-C_3N_4 component (~80.2%).[50] In the range of 25−350 °C, there was an obvious weight loss (~2.9%) in CN-300-0, which was attributed to the presence of hydroxyl and methyl groups (Figure S14).[51] Figure 3j shows the electron paramagnetic resonance (EPR) spectra of samples in the dark, where CN, CN-230-30, and CN-300-0 all exhibited a single Lorentzian line with a *g*-factor of 2.004, which originated from the unpaired electrons on the C atoms in heptazine rings. The intensity of the EPR signal for CN-300-0 was much higher than that for CN-230-30 and CN, which was attributed to the increased delocalization degree of the π-conjugated system caused by structure tuning.[52] It was also found that CN-300-0 exhibited more prominent signals corresponding to Q-PHI and methyl/hydroxyl groups compared with CN-230-30 in the aforementioned characterizations, indicating that ScMeOH was more effective and efficient for structure tuning g-C_3N_4 than SubMeOH. As discussed above, the modified g-C_3N_4 by the ScMeOH post-treatment was a kind of composite composed of g-C_3N_4 and Q-PHI, while abundant methyl and hydroxyl groups were grafted into modified g-C_3N_4.

The SCFs are commonly applied in nanosheet production by exfoliation of layered materials, and some phenomena concerning the exfoliation of aggregated g-C_3N_4 in ScMeOH were discovered. CN and CN-230-30 displayed a thick bulk with the aggregation of 2D sheets (Figure S15a,b), whereas some 2D thin sheets with wrinkles appeared in CN-300-0 (Figures 4a and S15c). Notably, Figure S15d shows the energy-dispersive X-ray (EDX) spectrum scanned from the scanning electron microscopy (SEM) image of CN-300-0 as well as the corresponding result of elemental content, and the inexistence of metal elements in modified g-C_3N_4 was consistent with the XPS results. Figure 4b,c presents the high-resolution transmission electron microscopy (TEM) image of CN-300-0, where only the lattice fringe of approximately 0.69 nm corresponding to the (100) plane of g-C_3N_4 was observed. It revealed the limited distribution range of the Q-PHI component compared with the g-C_3N_4 component. Figure 4d shows the size-distribution curves of all samples, and the average hydrodynamic diameters of CN, CN-230-30, and CN-300-0 were 1.86, 1.11, and 0.76 μm, respectively. The larger-size pristine g-C_3N_4 particles disinte-

grated into smaller-size segments, causing the intensity and position variations in size-distribution peak curves, and the ScMeOH displayed enhanced breakage and modification effect compared with SubMeOH, as repeatedly demonstrated by the aforementioned various characteristic results. Figure 4e shows the N_2 adsorption−desorption isotherms and the corresponding pore size-distribution curves of CN, CN-230-30, and CN-300-0. Due to the shearing and exfoliation effects of high-pressure and high-temperature fluids, the solvothermal post-treatment enlarged the Brunauer−Emmette−Teller (BET) surface area and generated more mesopores (Figure S16), which could increase the reactive sites and enhance the mass transfer in photocatalytic reaction. However, the BET surface area of CN-230-30 (24.1 $m^2 \cdot g^{-1}$) was larger than that of CN-300-0 (20.4 $m^2 \cdot g^{-1}$), indicating that there are more reasons for the enhanced photocatalytic activity in addition to the enlarged specific surface area of modified g-C_3N_4. The zeta-potential of the CN aqueous dispersion was negative, −22.5 mV, which became positive, 16.3 and 29.6 mV, for CN-230-30 and CN-300-0, respectively (Figure S17). In addition, the CN, CN-230-30, and CN-300-0 showed water contact angles of 32.3, 47.6, and 44.1°, respectively (Figure S18). The significant change of zeta potentials and water contact angles resulted from the appearance of abundant groups on the particle surface after solvothermal post-treatment. The ScMeOH post-treatment resulted in the exfoliation and phase transformation of g-C_3N_4, as well as causing methylation and hydroxylation reactions within g-C_3N_4, leading to a g-C_3N_4/Q-PHI isotype heterojunction photocatalyst with grafted methyl and hydroxyl groups.

Mechanism of Enhanced Photocatalytic H_2-Evolution Activity. The ScMeOH post-treatment successfully realized structure tuning for g-C_3N_4, and further analysis of optical properties, band alignment, and photogenerated charge carrier dynamics for samples could help understand the mechanism for enhanced photocatalytic H_2-evolution activity. Figure 5a shows the ultraviolet−visible (UV−vis) spectra of CN, CN-230-30, and CN-300-0. The CN exhibited an intrinsic absorption band below 450 nm due to a $\pi \rightarrow \pi^*$ electron transition, and the absorption edge of CN-230-30 red shifted slightly compared with that of CN. Moreover, an obvious new absorption band formed in the region from 450 to 700 nm in CN-300-0, which was ascribed to the $n \rightarrow \pi^*$ electron transition caused by long pairs of the grafted hydroxyl group in the Q-PHI component.[53,54]

Based on the atomic structure models constructed for g-C_3N_4 and Q-PHI, density functional theory (DFT) calculations have provided theoretical evidence that g-C_3N_4 and Q-PHI formed a type II alignment (Figures S19 and S20). In addition, the Q-PHI component was *in situ* derived from g-C_3N_4, thus forming an intimate type II isotype heterojunction between g-C_3N_4 and Q-PHI, which led to efficient charge separation within the modified g-C_3N_4.[55] As shown in Figure 5b, CN displayed a strong band-to-band emission peak at 463 nm, and the photoluminescence (PL) intensity for CN-230-30 significantly decreased. In contrast, CN-300-0 showed the weakest PL intensity, with two emission peaks located at 442 and 464 nm, corresponding to Q-PHI and g-C_3N_4. Figure 5c shows the time-resolved PL decay spectra and the calculated average PL lifetime (τ_{ave}). CN-300-0 had the shortest τ_{ave} (3.79 ns) compared with CN-230-30 (4.27 ns) and CN (5.64 ns). Both the decreased steady-state PL intensity and the shortened PL lifetime demonstrated that the recombination of photogenerated charge carrier was effectively suppressed.[56] In addition, from the electrochemical impedance spectra (EIS) results in Figure 5d, CN-300-0 had the smallest arc radius in its EIS results and CN-230-30 had a smaller arc radius than CN. These results suggested a lower charge-transfer impedance as well as a significant improvement in electron−hole separation and transfer rate of the modified g-C_3N_4 after the ScMeOH post-treatment. As seen in Figure 5e, the photocurrent of CN-300-0 and CN-230-30 were approximate and both were much higher than that of CN, implying an efficient separation and migration for the photogenerated charge carrier under light irradiation. The light irradiation could further enhance the EPR intensities of the photocatalyst owing to the presence of photogenerated electrons; the EPR spectra for samples in the dark and under light irradiation are shown in Figure 5f. Compared with the EPR signals in the dark, the EPR intensity enhancements under light irradiation in CN-230-30 and CN-300-0 were much higher than that of CN, indicating efficient generation of charge carrier in modified g-C_3N_4, which largely contributed to the enhanced photocatalytic activity.[57]

Based on the above analysis, a mechanism for the enhanced photocatalytic H_2-evolution activity for modified g-C_3N_4 by the ScMeOH post-treatment could be proposed and illustrated in Figure 6. According to the band structures of g-C_3N_4 and Q-PHI, a type II isotype heterojunction could be constructed between g-C_3N_4 and Q-PHI. The ordered and partial *in situ* phase transformation from g-C_3N_4 to Q-PHI formed a g-C_3N_4/Q-PHI composite coupled with chemical bonding, leading to an intimate heterojunction with a strong interfacial electric field that could effectively promote the separation and migration of charge carrier. In addition, the introduced abundant methyl and hydroxyl groups into the bulk structure of carbon nitride contributed to enhancing light absorption capacity, modulating the carrier dynamics, and increasing the active sites.[58] Furthermore, the exfoliation and linkage

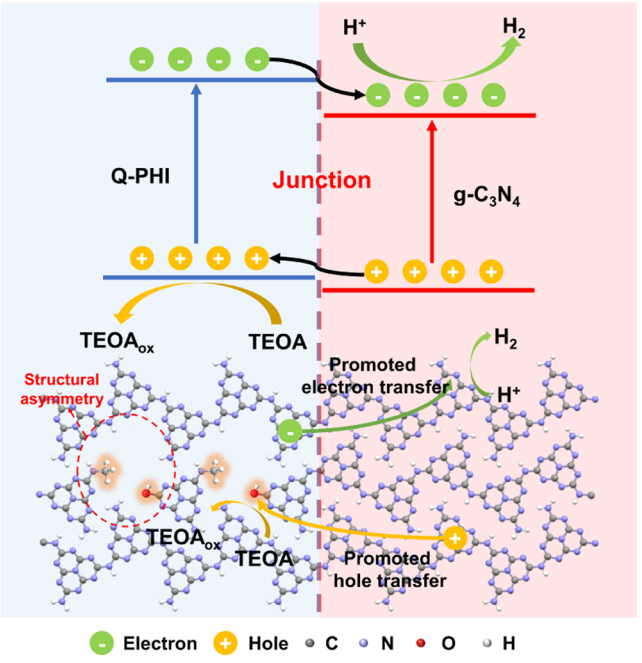

Figure 6. Schematic mechanism of the g-C_3N_4/Q-PHI isotype heterojunction with abundant grafted groups for photocatalytic H_2 evolution.

breakage effects of the ScMeOH post-treatment could also enlarge the surface area, thus enhancing the active sites. As a result, the synergistic promotions contributed to the excellent photocatalytic H_2-evolution activity of modified g-C_3N_4 by the ScMeOH post-treatment.

CONCLUSION

A ScMeOH post-treatment strategy was developed for structure tuning of bulk g-C_3N_4. The structural evolution of g-C_3N_4 and the mechanism of enhanced photocatalytic H_2-evolution activity for modified g-C_3N_4 were investigated. This strategy presented advantages of time-saving (less than 10 min), high yield (over 80%), and scalability due to the enhanced mass transfer and high reactivity of ScMeOH. It was found that ScMeOH was much more effective and efficient for the structure tuning of g-C_3N_4 compared with SubMeOH. During the ScMeOH post-treatment process, CH_3OH molecules diffused into the interlayers of g-C_3N_4 and underwent *N*-methylation and hydroxylation reactions with the intralayers, resulting in a partial phase transformation from g-C_3N_4 to Q-PHI with abundant methyl and hydroxyl groups. The modified g-C_3N_4 showed enhanced photocatalytic activity with an H_2-evolution rate 7.2 times that of pristine g-C_3N_4, which was attributed to the synergistic effects of isotype heterojunction construction, group modulation, and surface area increase. This work presents a post-treatment strategy for structure tuning of bulk g-C_3N_4 and serves as a practical case to demonstrate the unique properties of SCFs, showing great potential for large-scale synthesis of catalysts by SCF-based technology.

METHODS AND EXPERIMENTAL

To prepare pristine g-C_3N_4, melamine (5 g) was added in a covered ceramic crucible and calcined in a furnace under an air atmosphere at 550 °C for 4 h with a ramp rate of 5 °C min^{-1} from room temperature to 550 °C. The obtained powders were ground and denoted as CN.

The solvothermal post-treatment of g-C_3N_4 was carried out using a Hastelloy C276 tube reactor (11 mL). Pristine g-C_3N_4 (500 mg) was dispersed in CH_3OH (5 mL) in the reactor and then ultrasonically treated for 5 min. Subsequently, the reactor was tightly sealed. In order to replace the internal atmosphere of the reactor, high-pressure Ar (around 5 MPa) from a gas cylinder was injected into the reactor through an inlet gas valve until the internal pressure reached around 4 MPa, and then the gas in the reactor was released through an outlet gas valve. The internal atmosphere of the reactor was replaced three times based on the above operation; at the end, the internal pressure was controlled at around 2 MPa for the following reaction to avoid solvent vaporization and thus enhance heat transfer. Afterward, the reactor was heated in an electric furnace and held at a target temperature for a certain time and then removed from the heating furnace and quenched in a water bath (25 °C). After the gas was released in a fume hood, the solid product was separated from the obtained dispersion by vacuum filtration through a microfiltration membrane (Nylon66, 0.2 μm), then washed with water three times and ethanol one time in sequence, and finally dried at 60 °C for 6 h. The obtained modified g-C_3N_4 powders were designated as CN-*T*-*t*, where *T* was the post-treatment temperature and *t* was the residence time at the target post-treatment temperature.

For comparison, a series of control samples were prepared by the same procedure except that different alcohols, including EtOH, NPA, and IPA, were used in the solvothermal post-treatment of g-C_3N_4. The obtained modified g-C_3N_4 powders were designated as *F*−*T*−*t*, where *F* was the kind of alcohol, *T* was the post-treatment temperature, and *t* was the residence time at the target post-treatment temperature.

ASSOCIATED CONTENT

Supporting Information

The Supporting Information is available free of charge at https://pubs.acs.org/doi/10.1021/acsnano.4c03922.

Experimental sections on chemicals, sample characterization, gas and liquid products analysis, photocatalytic performance measurement, photoelectrochemical measurement, and computation details. Temperature and pressure curves, optical images, photocatalytic H_2-evolution rates and yields results, schematic diagram of structures, schematic diagram of *N*-methylation and hydroxylation reactions, temperature and pressure curves, contents of gas products results, schematic diagram of volume measurement using a graduated syringe, GC−MS results, XRD patterns, Gibbs free energies results, XPS results, TG curves, SEM images, BJH pore size-distribution curves, zeta-potential curves, photographs of water contact measurement, DFT results, and electronic band structure alignments. Preparation conditions and photocatalytic H2-evolution rates, comparison of represented solvothermal post-treatment strategies, Q-PHI model description, and XPS data (PDF)

AUTHOR INFORMATION

Corresponding Author

Jinwen Shi − *State Key Laboratory of Multiphase Flow in Power Engineering (MFPE), International Research Center for Renewable Energy (IRCRE), Xi'an Jiaotong University (XJTU), Xi'an 710049, China;* orcid.org/0000-0001-7291-2840; Email: jinwen_shi@mail.xjtu.edu.cn

Authors

Liuhao Mao − *State Key Laboratory of Multiphase Flow in Power Engineering (MFPE), International Research Center for Renewable Energy (IRCRE), Xi'an Jiaotong University (XJTU), Xi'an 710049, China*

Binjiang Zhai − *State Key Laboratory of Multiphase Flow in Power Engineering (MFPE), International Research Center for Renewable Energy (IRCRE), Xi'an Jiaotong University (XJTU), Xi'an 710049, China*

Xing Kang − *State Key Laboratory of Multiphase Flow in Power Engineering (MFPE), International Research Center for Renewable Energy (IRCRE), Xi'an Jiaotong University (XJTU), Xi'an 710049, China*

Bingru Lu − *State Key Laboratory of Multiphase Flow in Power Engineering (MFPE), International Research Center for Renewable Energy (IRCRE), Xi'an Jiaotong University (XJTU), Xi'an 710049, China*

Yanbing Liu − *State Key Laboratory of Multiphase Flow in Power Engineering (MFPE), International Research Center for Renewable Energy (IRCRE), Xi'an Jiaotong University (XJTU), Xi'an 710049, China*

Cheng Cheng − *State Key Laboratory of Multiphase Flow in Power Engineering (MFPE), International Research Center for Renewable Energy (IRCRE), Xi'an Jiaotong University (XJTU), Xi'an 710049, China*

Hui Jin − *State Key Laboratory of Multiphase Flow in Power Engineering (MFPE), International Research Center for Renewable Energy (IRCRE), Xi'an Jiaotong University (XJTU), Xi'an 710049, China;* orcid.org/0000-0001-9216-7921

Eric Lichtfouse − *State Key Laboratory of Multiphase Flow in Power Engineering (MFPE), International Research Center for Renewable Energy (IRCRE), Xi'an Jiaotong University (XJTU), Xi'an 710049, China;* orcid.org/0000-0002-8535-8073

Liejin Guo − *State Key Laboratory of Multiphase Flow in Power Engineering (MFPE), International Research Center for Renewable Energy (IRCRE), Xi'an Jiaotong University (XJTU), Xi'an 710049, China;* orcid.org/0000-0001-9412-3260

Complete contact information is available at: https://pubs.acs.org/10.1021/acsnano.4c03922

Author Contributions

†L.M. and B.Z. contributed equally to this work. The manuscript was written through contributions of all authors. All authors discussed the results and contributed to this manuscript.

Notes

The authors declare no competing financial interest.

ACKNOWLEDGMENTS

This work is supported by the Basic Science Center Program for Ordered Energy Conversion of the National Natural Science Foundation of China (No. 52488201), the National Natural Science Foundation of China (Nos. 52276213 and 52206276), the China Postdoctoral Science Foundation (No. 2022M712527), the Science and Technology Innovation Team Project of Shaanxi Province (No. S2023-ZC-TD-0071), and the Fundamental Research Funds for the Central Universities. The authors thank Jiamei Liu, Chuansheng Ma, Jiaxiang Sun, and Hang Guo from the Instrument Analysis Center of Xi'an Jiaotong University for their assistance with characterizations and corresponding analysis.

REFERENCES

(1) Guo, L.; Ou, Z.; Liu, Y.; Ge, Z.; Jin, H.; Ou, G.; Song, M.; Jiao, Z.; Jing, W. Technological Innovations on Direct Carbon Mitigation by Ordered Energy Conversion and Full Resource Utilization. *Carbon Neutrality* **2022**, *1*, 4.

(2) Song, H.; Luo, S.; Huang, H.; Deng, B.; Ye, J. Solar-Driven Hydrogen Production: Recent Advances, Challenges, and Future Perspectives. *ACS Energy Lett.* **2022**, *7*, 1043−1065.

(3) Han, Y.; Chen, Y.; Fan, R.; Li, Z.; Zou, Z. Promotion Effect of Metal Phosphides towards Electrocatalytic and Photocatalytic Water Splitting. *EcomMat* **2021**, *3*, No. e12097.

(4) Huang, Y.; Meng, L.; Xu, W.; Li, L. The Positive Versus Negative Effects of Defect Engineering for Solar Water Splitting: A review. *Adv. Funct. Mater.* **2023**, *33*, No. 2305940.

(5) Wang, Q.; Domen, K. Particulate Photocatalysts for Light-Driven Water Splitting: Mechanisms, Challenges, and Design Strategies. *Chem. Rev.* **2020**, *120*, 919−985.

(6) Zhou, Z.; Guo, W.; Yang, T.; Zheng, D.; Fang, Y.; Lin, X.; Hou, Y.; Zhang, G.; Wang, S. Defect and Nanostructure Engineering of Polymeric Carbon Nitride for Visible-Light-Driven CO_2 Reduction. *Chin. J. Struct. Chem.* **2024**, *43*, No. 100245.

(7) Tang, D.; Shao, C.; Jiang, S.; Sun, C.; Song, S. Graphitic C_2N_3: An Allotrope of g-C_3N_4 Containing Active Azide Pentagons as Metal-Free Photocatalyst for Abundant H_2 Bubble Evolution. *ACS Nano* **2021**, *15*, 7208−7215.

(8) Hu, S.; Qiao, P.; Yi, X.; Lei, Y.; Hu, H.; Ye, J.; Wang, D. Selective Photocatalytic Reduction of CO_2 to CO Mediated by Silver Single Atoms Anchored on Tubular Carbon Nitride. *Angew. Chem., Int. Ed.* **2023**, *62*, No. e2023045.

(9) Zhao, D.; Wang, Y.; Dong, C.; Huang, Y.; Chen, J.; Xue, F.; Shen, S.; Guo, L. Boron-Doped Nitrogen-Deficient Carbon Nitride-Based Z-Scheme Heterostructures for Photocatalytic Overall Water Splitting. *Nat. Energy* **2021**, *6*, 388−397.

(10) Bu, X.; Li, J.; Yang, S.; Sun, J.; Deng, Y.; Yang, Y.; Wang, G.; Peng, Z.; He, P.; Wang, X.; Ding, G.; Yang, J.; Xie, X. Surface Modification of C_3N_4 through Oxygen-Plasma Treatment: A Simple Way toward Excellent Hydrophilicity. *ACS Appl. Mater. Interfaces* **2016**, *8*, 31419−31425.

(11) Cheng, C.; Mao, L.; Kang, X.; Dong, C.; Huang, Y.; Shen, S.; Shi, J.; Guo, L. A High-Cyano Groups-Content Amorphous-Crystalline Carbon Nitride Isotype Heterojunction Photocatalyst for High-Quantum-Yield H_2 Production and Enhanced CO_2 Reduction. *Appl. Catal., B* **2023**, *331*, No. 122733.

(12) Zheng, D.; Wang, Q.; Pan, Z.; Wang, S.; Hou, Y.; Zhang, G. Poly(triazine imide) Nanospheres with Spatially Exposed Prismatic Facets for Photocatalytic Overall Water Splitting. *Sci. China Mater.* **2024**, 1−7, DOI: 10.1007/s40843-023-2752-9.

(13) Yu, S.; Li, J.; Zhang, Y.; Li, M.; Dong, F.; Zhang, T.; Huang, H. Local Spatial Charge Separation and Proton Activation Induced by Surface Hydroxylation Promoting Photocatalytic Hydrogen Evolution of Polymeric Carbon Nitride. *Nano Energy* **2018**, *50*, 383−392.

(14) Liu, Y.; Shi, J.; Jin, H.; Guo, L. Chemical Recycling Methods for Managing Waste Plastics: A Review. *Environ. Chem. Lett.* **2024**, *22*, 149−169.

(15) Padmajan Sasikala, S.; Poulin, P.; Aymonier, C. Prospects of Supercritical Fluids in Realizing Graphene-Based Functional Materials. *Adv. Mater.* **2016**, *28*, 2663−2691.

(16) Hanabata, S.; Kusada, K.; Yamamoto, T.; Toriyama, T.; Matsumura, S.; Kawaguchi, S.; Kubota, Y.; Nishida, Y.; Haneda, M.; Kitagawa, H. Denary High-Entropy Oxide Nanoparticles Synthesized by a Continuous Supercritical Hydrothermal Flow Process. *J. Am. Chem. Soc.* **2024**, *146*, 181−186.

(17) Zhang, B.; Wang, S.; Li, Y.; Sun, P.; Yang, C.; Wang, D.; Liu, L. Review: Phase Transition Mechanism and Supercritical Hydrothermal Synthesis of Nano Lithium Iron Phosphate. *Ceram. Int.* **2020**, *46*, 27922−27939.

(18) Darr, J. A.; Zhang, J.; Makwana, N. M.; Weng, X. Continuous Hydrothermal Synthesis of Inorganic Nanoparticles: Applications and Future Directions. *Chem. Rev.* **2017**, *117*, 11125−11238.

(19) Gong, J.; Zhao, G.; Feng, J.; An, Y.; Li, T.; Zhang, L.; Li, B.; Qian, Z. Controllable Phosphorylation Strategy for Free-Standing Phosphorus/Nitrogen Cofunctionalized Porous Carbon Monoliths as High-Performance Potassium Ion Battery Anodes. *ACS Nano* **2020**, *14*, 14057−14069.

(20) Sun, Z.; Liu, Z.; Han, B.; Wang, Y.; Du, J.; Xie, Z.; Han, G. Fabrication of Ruthenium-Carbon Nanotube Nanocomposites in Supercritical Water. *Adv. Mater.* **2005**, *17*, 928−932.

(21) Liu, Y.; Zhang, M.; Zhang, Y.; Liu, Y.; Wang, L.; Li, X.; Xue, M.; Li, B.; Tao, X. $Li_4Ti_5O_{12}/TiO_2$ Dual-Phase Anode Materials Synthesized in Supercritical Water−Methanol System and Investigations on Its Superior Electrochemical Performance for Lithium-Ion Batteries. *J. Supercrit. Fluids* **2019**, *154*, No. 104596.

(22) Li, S.; Zhu, B.; Wang, W.; Zhang, H.; Li, Q. Efficient and Stable Supercritical-Water-Synthesized Ni-Based Catalysts for Supercritical Water Gasification. *J. Supercrit. Fluids* **2020**, *160*, No. 104790.

(23) Li, L.; Zheng, X.; Wang, J.; Sun, Q.; Xu, Q. Solvent-Exfoliated and Functionalized Graphene with Assistance of Supercritical Carbon Dioxide. *ACS Sustainable Chem. Eng.* **2013**, *1*, 144−151.

(24) Wang, N.; Wei, F.; Qi, Y.; Li, H.; Lu, X.; Zhao, G.; Xu, Q. Synthesis of Strongly Fluorescent Molybdenum Disulfide Nanosheets for Cell-Targeted Labeling. *ACS Appl. Mater. Interfaces* **2014**, *6*, 19888−19894.

(25) Zhou, Y.; Xu, Q.; Ge, T.; Zheng, X.; Zhang, L.; Yan, P. Accurate Control of VS_2 Nanosheets for Coexisting High Photoluminescence and Photothermal Conversion Efficiency. *Angew. Chem., Int. Ed.* **2020**, *59*, 3322−3328.

(26) Tong, X.; Du, L.; Xu, Q. Tough, Adhesive and Self-Healing Conductive 3D Network Hydrogel of Physically Linked Function-

alized-Boron Nitride/Clay/Poly(*N*-isopropylacrylamide). *J. Mater. Chem. A* **2018**, *6*, 3091−3099.
(27) Tayyebi, A.; Akhavan, O.; Lee, B.-K.; Outokesh, M. Supercritical Water in Top-Down Formation of Tunable-Sized Graphene Quantum Dots Applicable in Effective Photothermal Treatments of Tissues. *Carbon* **2018**, *130*, 267−272.
(28) Liu, W.; Xu, Q.; Cui, W.; Zhu, C.; Qi, Y. CO_2-Assisted Fabrication of Two-Dimensional Amorphous Molybdenum Oxide Nanosheets for Enhanced Plasmon Resonances. *Angew. Chem.* **2017**, *129*, 1622−1626.
(29) Ren, Y.; Xu, Q.; Wang, C.; Zheng, X.; Jia, Y.; Qi, Y.; Zhou, Y.; Yang, X.; Zhang, Z. CO_2-Assisted Solution-Phase Selective Assembly of 2D WS_2−WO_3 H_2O and 1T−2H MoS_2 to Desirable Complex Heterostructures. *ChemNanoMat* **2017**, *3*, 632−638.
(30) Zheng, X.; Guo, Z.; Zhang, G.; Li, H.; Zhang, J.; Xu, Q. Building a Lateral/Vertical 1T−2H MoS_2/Au Heterostructure for Enhanced Photoelectrocatalysis and Surface Enhanced Raman Scattering. *J. Mater. Chem. A* **2019**, *7*, 19922−19928.
(31) Gao, B.; Li, L.; Chen, Z.; Xu, Q. Pressure Coupled Lanthanide Ion Doping to Enhance Optical Properties in $BaTiO_3$. *Small* **2024**, *20*, No. 2308427.
(32) Sandhiya, M.; Veerappan, U. K. K.; Sathish, M. Crumpled B, F Co-Doped Graphene Nanosheets for the Fabrication of All-Solid-State Flexible Supercapacitors. *Chem. Commun.* **2021**, *57*, 8336−8339.
(33) Suresh Balaji, S.; Sandhiya, M.; Sathish, M. Enhanced Electrochemical Performance of Supercritical Fluid Aided P-Doped Graphene Nanoflakes by I^{3-}/I^- Redox Couple. *J. Energy Storage* **2021**, *33*, No. 102085.
(34) Kang, X.; Mao, L.; Shi, J.; Liu, Y.; Zhai, B.; Xu, J.; Jiang, Y.; Lichtfouse, E.; Jin, H.; Guo, L. Supercritical Carbon Dioxide Systems for Sustainable and Efficient Dissolution of Solutes: A Review. *Environ. Chem. Lett.* **2024**, *22*, 815−839.
(35) Shi, J.; Kang, X.; Mao, L.; Jiang, Y.; Zhao, S.; Liu, Y.; Zhai, B.; Jin, H.; Guo, L. Supercritical CO_2-Applied Equipment for Chemical Synthesis and Transformation: Current Status and Perspectives. *Chem. Eng. J.* **2023**, *459*, No. 141608.
(36) Abdulagatov, I. M.; Polikhronidi, N. G.; Abdurashidova, A.; Kiselev, S. B.; Ely, J. F. Thermodynamic Properties of Methanol in the Critical and Supercritical Regions. *Int. J. Thermophys.* **2005**, *26*, 1327−1368.
(37) Budi Nursanto, E.; Nugroho, A.; Hong, S.-A.; Kim, S. J.; Yoon Chung, K.; Kim, J. Facile Synthesis of Reduced Graphene Oxide in Supercritical Alcohols and its Lithium Storage Capacity. *Green Chem.* **2011**, *13*, 2714−2718.
(38) Seo, M.; Yoon, D.; Hwang, K. S.; Kang, J. W.; Kim, J. Supercritical Alcohols as Solvents and Reducing Agents for the Synthesis of Reduced Graphene Oxide. *Carbon* **2013**, *64*, 207−218.
(39) Leng, Y.; Gao, Y.; Wang, W.; Zhao, Y. Continuous Supercritical Solvothermal Synthesis of TiO_2−Pristine-Graphene Hybrid as the Enhanced Photocatalyst. *J. Supercrit. Fluids* **2015**, *103*, 115−121.
(40) Sasikala, S. P.; Henry, L.; Yesilbag Tonga, G.; Huang, K.; Das, R.; Giroire, B.; Marre, S.; Rotello, V. M.; Penicaud, A.; Poulin, P.; Aymonier, C. High Yield Synthesis of Aspect Ratio Controlled Graphenic Materials from Anthracite Coal in Supercritical Fluids. *ACS Nano* **2016**, *10*, 5293−5303.
(41) Li, S.; Cheng, W.; Liu, X.; Wang, C.; Li, W.; Yu, S. Supercritical Methanol Synthesis, Phase Evolution and Formation Mechanism of $Cu_{1.8}S$ and Cu_9S_5/CuS Complex Microcrystal. *J. Supercrit. Fluids* **2018**, *133*, 429−436.
(42) Wang, L.; Xu, W.; Yang, J. Applications of Supercritical Methanol in Chemical Reactions. *Prog. Chem.* **2010**, *22*, 796−802.
(43) Xu, Y.; Musumeci, V.; Aymonier, C. Chemistry in Supercritical Fluids for the Synthesis of Metal Nanomaterials. *React. Chem. Eng.* **2019**, *4*, 2030−2054.
(44) Mao, L.; Lu, B.; Shi, J.; Zhang, Y.; Kang, X.; Chen, Y.; Jin, H.; Guo, L. Rapid High-Temperature Hydrothermal Post Treatment on Graphitic Carbon Nitride for Enhanced Photocatalytic H_2 Evolution. *Catal. Today* **2023**, *409*, 94−102.
(45) Lotsch, B. V.; Döblinger, M.; Sehnert, J.; Seyfarth, L.; Senker, J.; Oeckler, O.; Schnick, W. Unmasking Melon by a Complementary Approach Employing Electron Diffraction, Solid-State NMR Spectroscopy, and Theoretical Calculations—Structural Characterization of a Carbon Nitride Polymer. *Chem. - Eur. J.* **2007**, *13*, 4969−4980.
(46) Zhang, J.; Ye, G.; Zhang, C.; Pan, Z.; Wang, S.; Zhang, G.; Wang, X. Heptazine-Based Ordered−Distorted Copolymers with Enhanced Visible-Light Absorption for Photocatalytic Hydrogen Production. *ChemSusChem* **2022**, *15*, No. 202201616.
(47) Lee, J.; Kim, C.; Cheong, J. Y.; Kim, I. D. An Angstrom-Level d-Spacing Control of Graphite Oxide Using Organofillers for High-Rate Lithium Storage. *Chem.* **2022**, *8*, 2393−2409.
(48) Zhao, S.; Zhao, X.; Ouyang, S.; Zhu, Y. Polyoxometalates Covalently Combined with Graphitic Carbon Nitride for Photocatalytic Hydrogen Peroxide Production. *Catal. Sci. Technol.* **2018**, *8*, 1686−1695.
(49) Yang, Q.; Chen, C.; Zhang, Q.; Zhang, Z.; Fang, X. Molecular Engineering of Supramolecular Precursor to Modulate g-C_3N_4 for Boosting Photocatalytic Hydrogen Evolution. *Carbon* **2020**, *164*, 337−348.
(50) Silva, I. F.; Rios, R. D. F.; Savateev, O.; Teixeira, I. F. Carbon Nitride-Based Nanomaterials as a Sustainable Catalyst for Biodiesel Production. *ACS Appl. Nano Mater.* **2023**, *6*, 9718−9727.
(51) Wu, X.; Wang, X.; Wang, F.; Yu, H. Soluble g-C_3N_4 Nanosheets: Facile Synthesis and Application in Photocatalytic Hydrogen Evolution. *Appl. Catal., B* **2019**, *247*, 70−77.
(52) Xia, P.; Cheng, B.; Jiang, J.; Tang, H. Localized π-Conjugated Structure and EPR Investigation of g-C_3N_4 Photocatalyst. *Appl. Surf. Sci.* **2019**, *487*, 335−342.
(53) Song, B.; Zhang, M.; Hou, S.; Liang, H.; Li, Q.; Yang, J. Synthesis of Carbon Nitride Nanosheets with n→π^* Electronic Transition for Boosting Photocatalytic CO_2 Reduction. *J. Electrochem. Soc.* **2023**, *170*, No. 036502.
(54) Zhang, G.; Li, G.; Lan, Z.-A.; Lin, L.; Savateev, A.; Heil, T.; Zafeiratos, S.; Wang, X.; Antonietti, M. Optimizing Optical Absorption, Exciton Dissociation, and Charge Transfer of a Polymeric Carbon Nitride with Ultrahigh Solar Hydrogen Production Activity. *Angew. Chem.* **2017**, *129*, 13630−13634.
(55) Shen, S.; Chen, J.; Wang, Y.; Dong, C.; Meng, F.; Zhang, Q.; Huangfu, Y.; Lin, Z.; Huang, Y.; Li, Y.; Li, M.; Gu, L. Boosting Photocatalytic Hydrogen Production by Creating Isotype Heterojunctions and Single-Atom Active Sites in Highly-Crystallized Carbon Nitride. *Sci. Bull.* **2022**, *67*, 520−528.
(56) Shao, M.; Chen, W.; Ding, S.; Lo, K. H.; Zhong, X.; Yao, L.; Ip, W. F.; Xu, B.; Wang, X.; Pan, H. WX_y/g-C_3N_4 (WX_y = W_2C, WS_2, or W_2N) Composites for Highly Efficient Photocatalytic Water Splitting. *ChemSusChem* **2019**, *12*, 3355−3362.
(57) Zhang, J.; Zhang, G.; Chen, X.; Lin, S.; Möhlmann, L.; Dolega, G.; Lipner, G.; Antonietti, M.; Blechert, S.; Wang, X. Co-monomer Control of Carbon Nitride Semiconductors to Optimize Hydrogen Evolution with Visible Light. *Angew., Chem. Int. Ed.* **2012**, *51*, 3183−3187.
(58) Wang, N.; Cheng, L.; Liao, Y.; Xiang, Q. Effect of Functional Group Modifications on the Photocatalytic Performance of g-C_3N_4. *Small* **2023**, *19*, No. e2300109.

Supporting Information for

Supercritical CH_3OH-triggered isotype heterojunction and groups in g-C_3N_4 for enhanced photocatalytic H_2 evolution

Liuhao Mao†, Binjiang Zhai†, Jinwen Shi*, Xing Kang, Bingru Lu, Yanbing Liu, Cheng Cheng, Hui Jin, Eric Lichtfouse, Liejin Guo

State Key Laboratory of Multiphase Flow in Power Engineering (MFPE), International Research Center for Renewable Energy (IRCRE), Xi'an Jiaotong University (XJTU), 28 West Xianning Road, Xi'an 710049, China

† *These authors contribute equally.*

* *Corresponding author. E-mail addresses: jinwen_shi@mail.xjtu.edu.cn (J. Shi)*

Experimental section

Chemicals

All reagents were of analytical grade and were used without further purification. Melamine ($C_3H_6N_6$), methanol (MeOH, CH_3OH), ethanol (EtOH, C_2H_5OH), n-propanol (NPA, C_3H_7OH), isopropanol (IPA, C_3H_7OH) and triethanolamine (TEOA, $C_6H_{15}NO_3$) were purchased from Sinopharm Chemical Reagent Co., Ltd. Chloroplatinic acid hexahydrate ($H_2PtCl_6 \cdot 6H_2O$) was purchased from Sigma-Aldrich Co., Ltd., and was made into aqueous solution with an equivalent Pt content of 0.775 mg·mL^{-1}. Argon gas (Ar, 99.999% purity) and Helium gas (He, 99.9999% purity) was purchased from Shaanxi Xinghua Group Co., Ltd. Deionized water with a resistivity of 18.25 MΩ·cm was used in experiments.

Characterizations

X-ray diffraction (XRD) patterns were obtained by a diffractometer (PANalytical, X'pert MPD Pro, Netherlands) by a scan rate of 10°·min^{-1} in the 2θ range from 5 to 80° under Ni-filtered Cu Kα irradiation (λ = 1.5406 Å). Fourier transform infrared (FTIR) spectra were recorded by an FTIR spectrophotometer (Bruker, Vertex 70, Germany) with using the KBr pellet technique. N_2 adsorption–desorption isotherms were recorded by an accelerated surface area and porosimetry analyzer (Micromeritics, ASAP 2460, USA) for Brunauer–Emmette–Teller (BET) specific surface area and Barrett–Joyner–Halenda (BJH) porosity analysis, and all materials were degassed in vacuum at 423 K for 12 h before N_2 adsorption analysis. X-ray photoelectron spectra (XPS) were recorded by an X-ray photoelectron spectroscope (Kratos, Axis Ultra DLD, Japan) using a monochromatic Al Kα line source ($h\nu$ = 1486.69 eV), and the adventitious C 1s peak at 284.8 eV was applied as reference. Ultraviolet–visible (UV–Vis) spectra were collected by an ultraviolet–visible–near-infrared spectrophotometer (Hitachi, U-4100, Japan) with $BaSO_4$ reference and diffuse reflectance mode in the range from 300 to 800 nm. Scanning electron microscopy (SEM) images and energy-dispersive X-ray (EDX) spectra were recorded by a field-emission scanning electron microscope (JEOL, JSM-7800F, Japan). Transmission electron microscopy (TEM) images were obtained from a

transmission electron microscope (Thermo Scientific, Talos L120C G2, USA) with an accelerating voltage of 120 kV. Zeta potentials and dynamic light scattering (DLS) sizes were recorded by zeta potentials instrument (Malvern Instruments, Zetasizer Nano ZS, England), and the powders were dispersed in pure water (c = 0.5 mg·mL^{-1}, pH = 7) for measurement. Element contents were obtained using an elemental analyzer (EA, Euro Vector, EA3000, Italy) with He as carrier gas and O_2 as reaction gas. Photoluminescence (PL) spectra were obtained from a fluorescence spectrophotometer (Edinburg Instruments, FLS1000, England) at room temperature, and the steady-state and time-resolved PL signals were obtained under the excitation wavelengths of 370 and 405 nm, respectively. Thermogravimetric (TG) curves were recorded by a thermal analyzer (Mettler Toledo, TGA/DSC3+, Switzerland) in the range from 25 to 800^{o}C. Solid-state ^{13}C nuclear magnetic resonance (NMR) spectra were taken on an NMR spectrometer JEOL, JNM-ECZ400R/S1, Japan). Electron paramagnetic resonance (EPR) test was performed on an EPR spectrometer (Bruker, A300-9.5/12/S/W, Germany) at room temperature both in the dark and under light irradiation. The measurement of contact angle was performed on a commercial contact angle system (Shanghai Zhongchen, SL200B China) with 6 μL of water droplet as the indicator, and the samples (50 mg) were prepared as tablets with flat surface by a preforming machine.

Analysis of gas and liquid products from solvothermal posttreatment

The gas products were collected by a gas pocket for further analysis, and the compositions of gas products were analyzed by gas chromatography (GC) using a gas chromatograph (Agilent, 7890A, USA) equipped with a thermal conductivity detector and a C-2000 capillary column, and Ar was used as carrier gas.

The liquid products were filtrated and collected through a filter (0.22 μm) to remove the particle photocatalysts. The compositions of liquid products were analyzed by the combination of gas chromatograph (GC, Agilent, HP 6980GC, USA)–mass spectrometer (MS, Agilent, HP 5973MSD, USA), and He was used as carrier gas.

Photocatalytic performance measurements

Photocatalytic H_2-evolution measurements were carried out in a Pyrex glass reactor (105 mL), and an Xe lamp (300 W) was used as the light source to provide visible-light

irradiation after being equipped with a 400 nm cut-off filter. Photocatalyst (50 mg) was dispersed in TEOA aqueous solution (10 vol%, 80 mL), and then H_2PtCl_6 aqueous solution (0.645 mL, corresponding to 0.5 mg Pt) was added into the dispersion. The reactor was purged with Ar for 30 min to eliminate O_2 before the photocatalytic reaction. During the measurement, the solution was maintained at 35°C by circulating water and was stirred constantly. The evolved gas was detected by GC using a gas chromatograph (North Point, NP-GC-901A, China) with a thermal conductivity detector and a TDX-01 column, and Ar as carrier gas.

The measurement of apparent quantum yield (AQY) was carried out under the irradiation of light with different wavelengths, i.e., 400, 420, 450 475 and 500 nm, realized by band-pass filters. The light intensities were recorded by a photoradiometer (PerfectLight, PL-MW 2000, China).

The AQY values were obtained as follows.

$$\text{AQY (\%)} = \frac{\text{number of evolved hydrogen molecules} \times 2}{\text{number of incident photons}} \times 100\%$$

Photoelectrochemical measurements

Photoelectrochemical measurements were carried out in a three-electrode chemical cell, in which the electrolyte, the counter electrode and the reference electrode were Na_2SO_4 aqueous solution (0.5 M), Pt foil and Ag/AgCl, respectively. The working electrode was fabricated by dropping the sample dispersion onto a glassy carbon electrode (0.2 mg·cm^{-2}). Transient photocurrent curves were recorded under chopped light irradiation at an applied voltage of +0.6 V vs Ag/AgCl. Electrochemical impedance spectra (EIS) were measured from 100 kHz to 1 Hz at an applied voltage of +0.6 V vs Ag/AgCl.

Computational details

Molecular dynamics simulations, including geometry optimization and transition state search, and frequency calculation, were realized with the Dmol3 program in Materials Studio using the m-GGA/M06-L method with DND basis.

Density functional theory (DFT) calculations were accomplished by the Vienna ab-initio Simulation Package (VASP) codes. The core electrons were described by

projected augmented wave (PAW) pseudo-potentials. The exchange and correlation effects of valence electrons were treated by the generalized gradient approximation (GGA) using the functional developed by Perdew–Burke–Ernzerhof (PBE). The g-C_3N_4 and Q-PHI were fully relaxed by the method of a conjugate-gradient algorithm with the criterion of force convergence in 0.02 eV $Å^{-1}$ and total energy convergence within 10^{-5} eV. The basis sets of plane waves were cut-off by 500 eV, and k-points mesh of g-C_3N_4 and Q-PHI were generated by the Gamma center method for structure relaxation. As for the band structure computation, due to the ripple of the g-C_3N_4 and Q-PHI, the k path was changed from G-X-H_1-C-H-Y-G of the Q-PHI to the G-X-S-Y-G of the g-C_3N_4

Supplementary figures

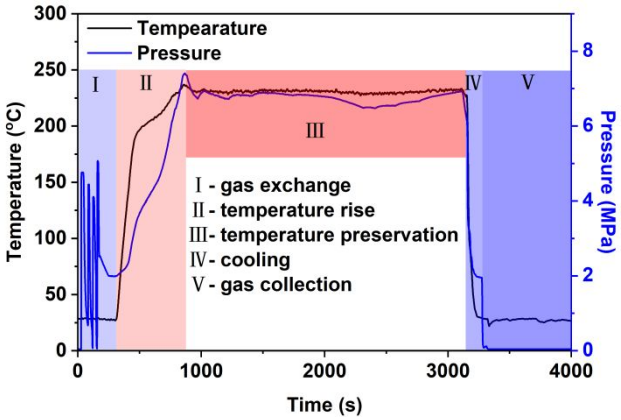

Figure S1. Temperature (left axis) and pressure (right axis) curves for solvothermal posttreatment process.

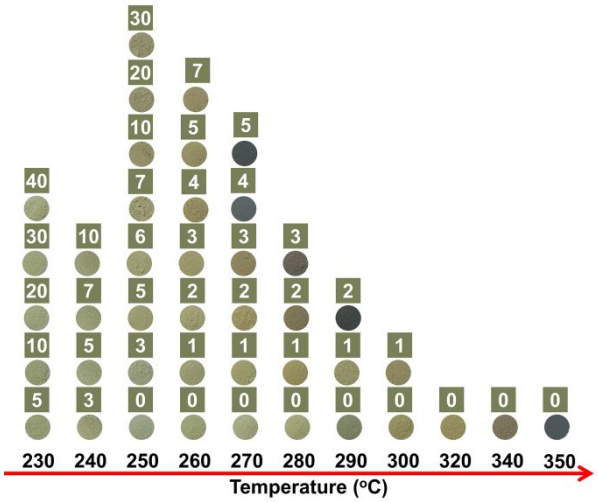

Figure S2. Optical images for CN-*T*-*t* samples. The numbers above the sample images represented the values of *t* (unit: min).

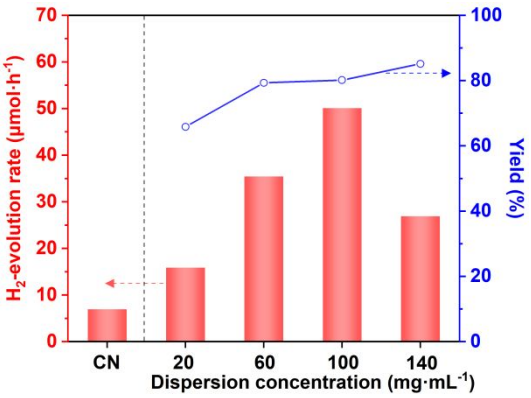

Figure S3. Photocatalytic H_2-evolution rates (left axis) and yields (right axis) for modified g-C_3N_4 obtained from ScMeOH solvothermal posttreatment (treatment temperature: 300°C, residence time: 0 min) with different dispersion concentrations.

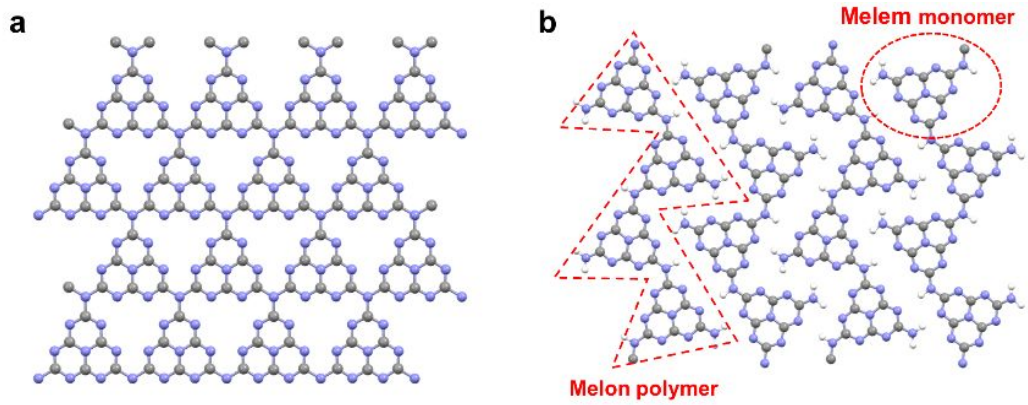

Figure S4. Schematic diagram about the basic structure for (a) ideal g-C_3N_4 and (b) amorphous g-C_3N_4.

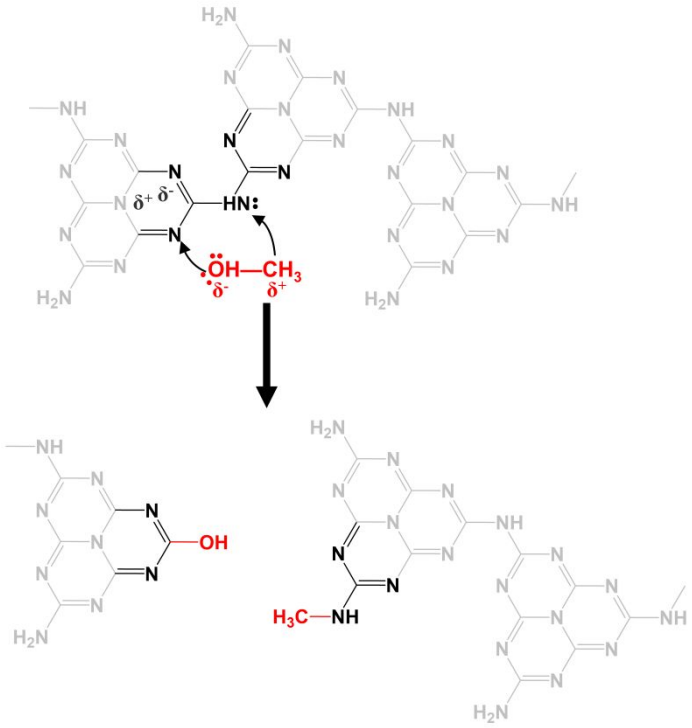

Figure S5. Proposed mechanism about the breakage of C–N bonds between NH-bridged melem monomers through *N*-methylation and hydroxylation reactions by ScMeOH posttreatment.

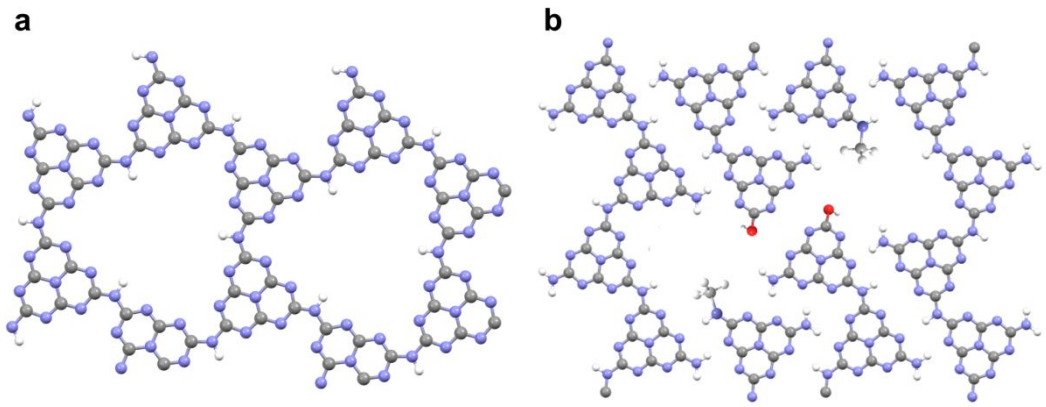

Figure S6. Schematic diagram about the basic structure for (a) PHI and (b) Q-PHI.

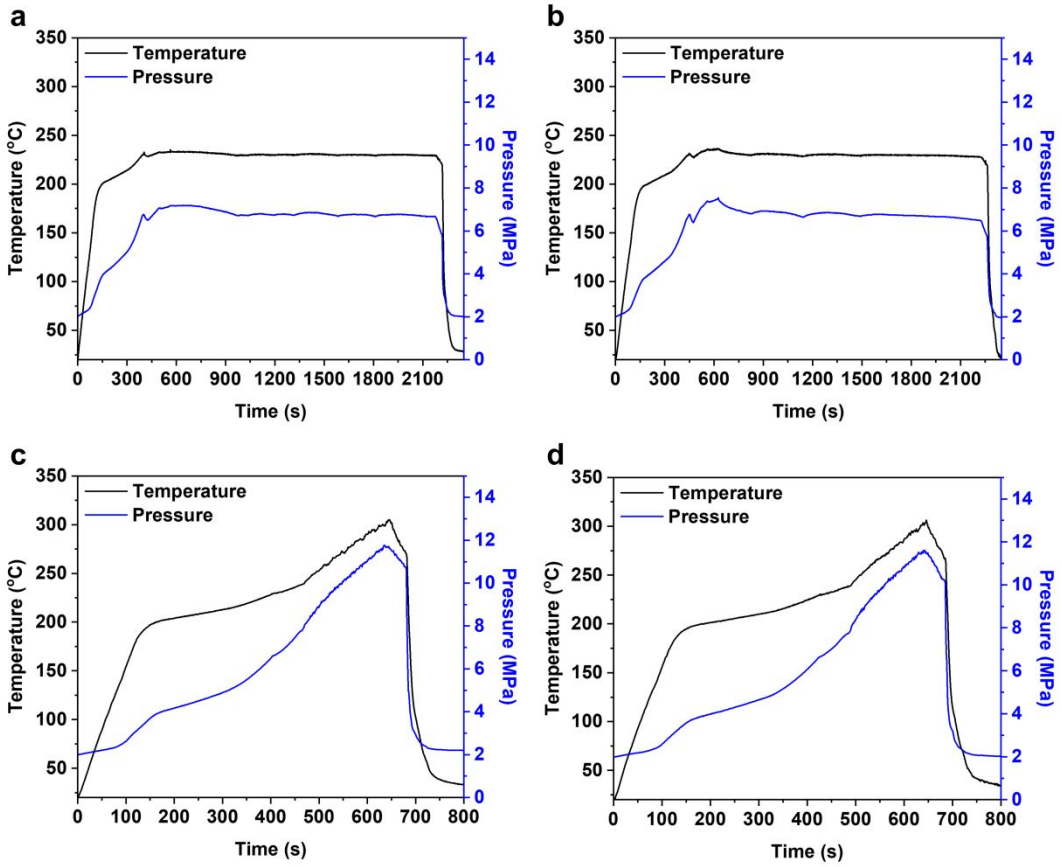

Figure S7. Temperature (left axis) and pressure (right axis) curves for the posttreatment process of (a) MeOH-230-30, (b) CN-230-30, (c) MeOH-300-0 and (d) CN-300-0. MeOH-230-30 and MeOH-300-0 were blank runs in the absence of g-C_3N_4 while other conditions were the same.

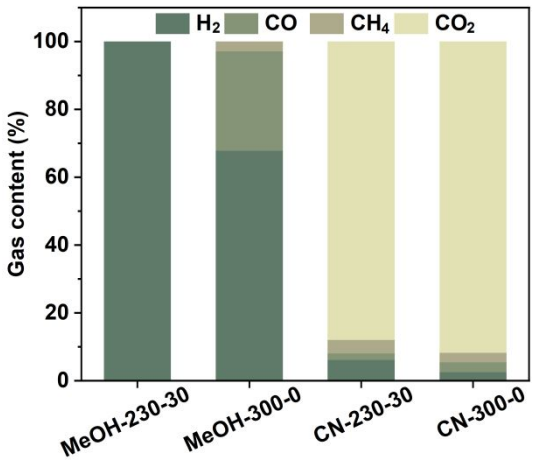

Figure S8. Contents of gas products from MeOH-230-30, MeOH-300-0, CN-230-30 and CN-300-0.

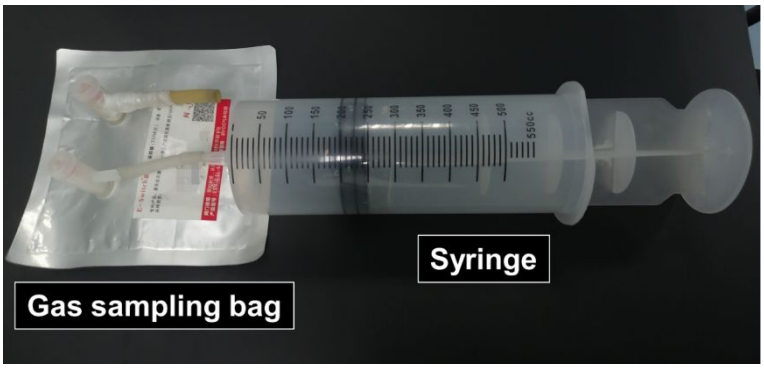

Figure S9. Volume measurement using a graduated syringe.

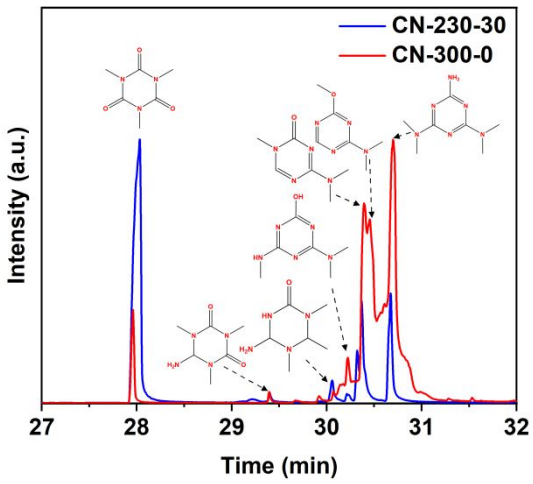

Figure S10. GC–MS results of the main compounds in liquid products from CN-230-30 and CN-300-0.

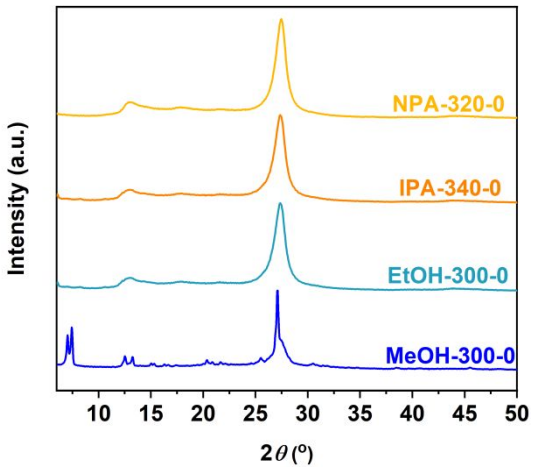

Figure S11. XRD patterns for MeOH-300-0, EtOH-300-0, IPA-340-0 and NPA-320-0.

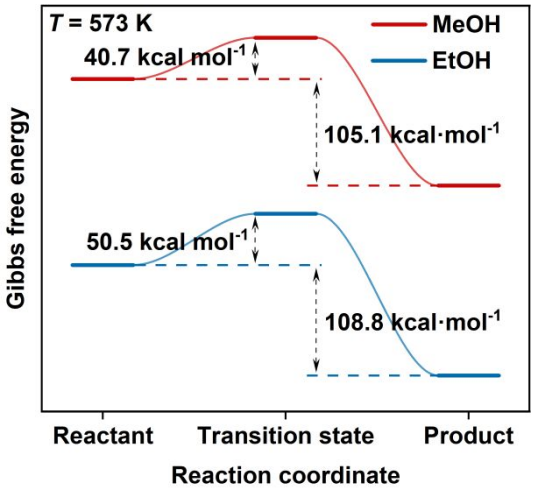

Figure S12. Gibbs free energies calculated by molecular dynamics simulations for the formation pathways of Q-PHI by reactions with MeOH and EtOH.

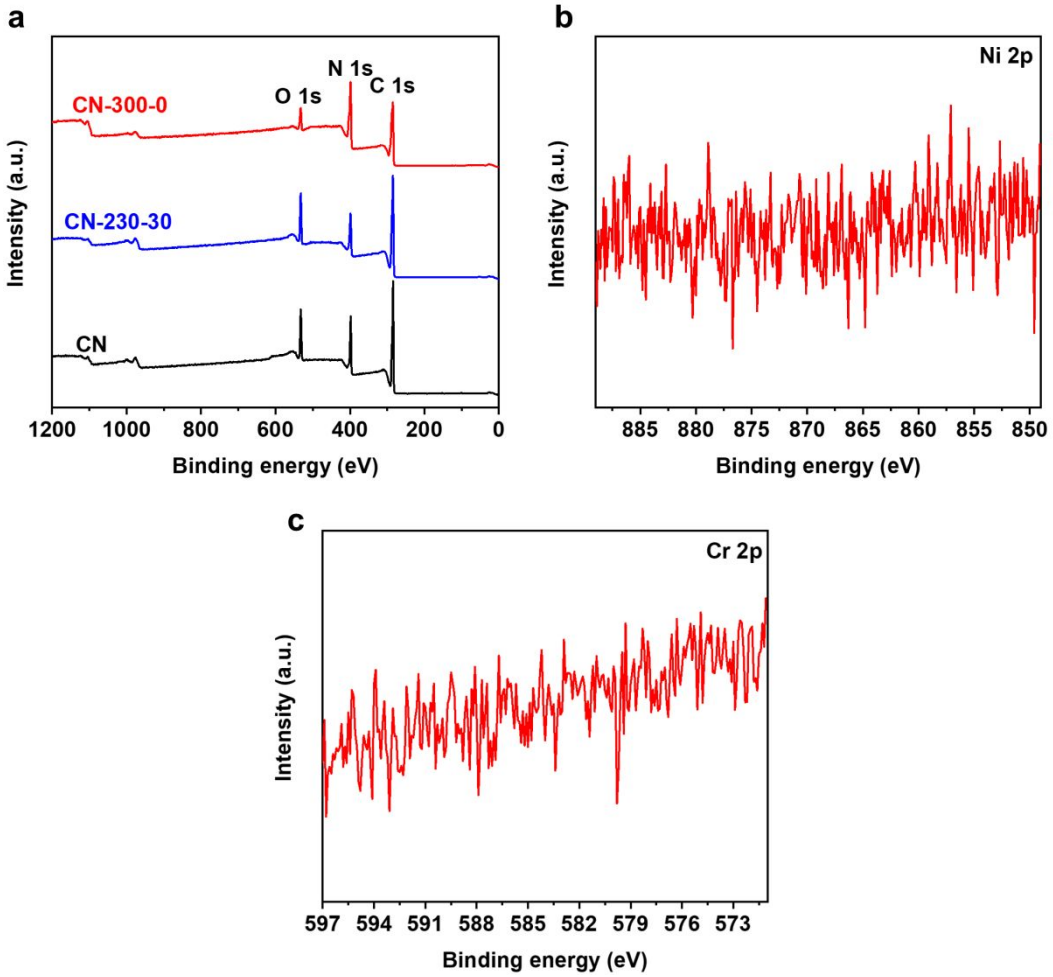

Figure S13. (a) Survey-scan XPS for CN, CN-230-30 and CN-300-0. High-resolution XPS of (b) Ni 2p and (c) Cr 2p orbitals for CN-300-0.

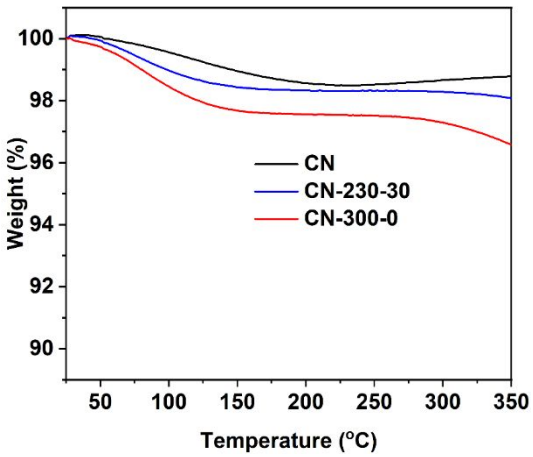

Figure S14. TG curves for CN, CN-230-30 and CN-300-0 from 25 to 350°C.

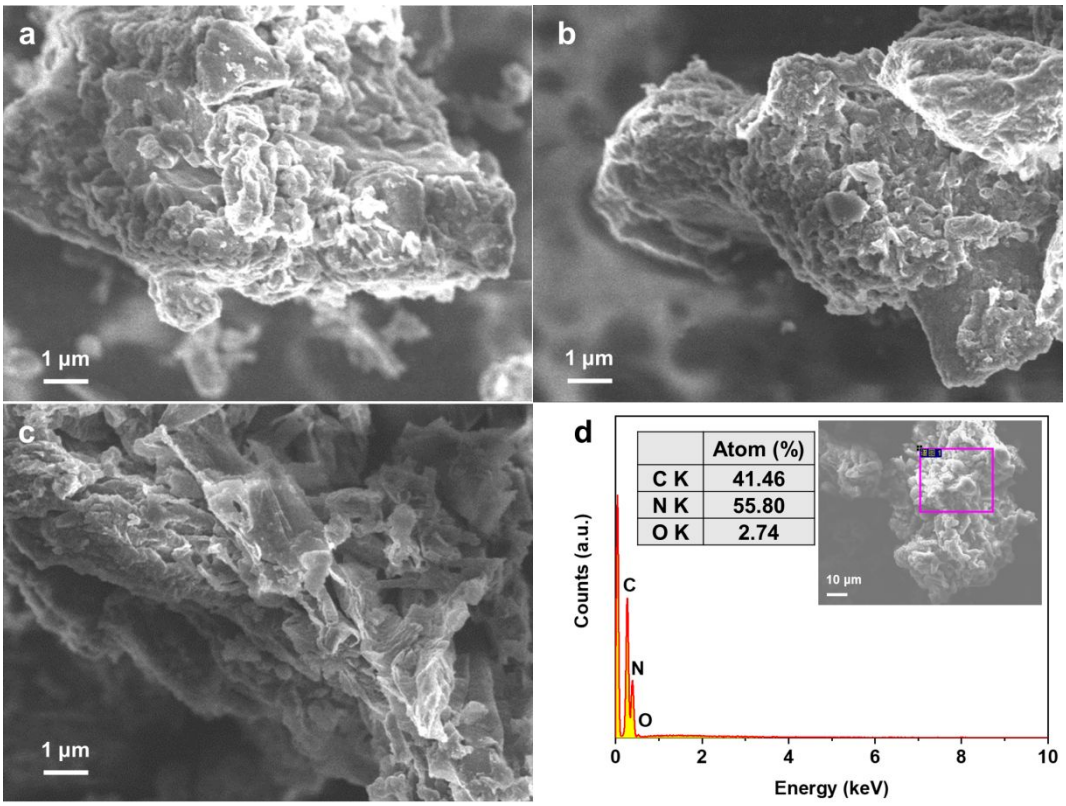

Figure S15. SEM images for (a) CN, (b) CN-230-30, (c) CN-300-0. (d) EDX spectrum and (table from the inset) corresponding result of elemental content detected from the selected area in (figure from the inset) SEM image for CN-300-0. Scale bar: (a–c) 1 μm, (d) 10 μm.

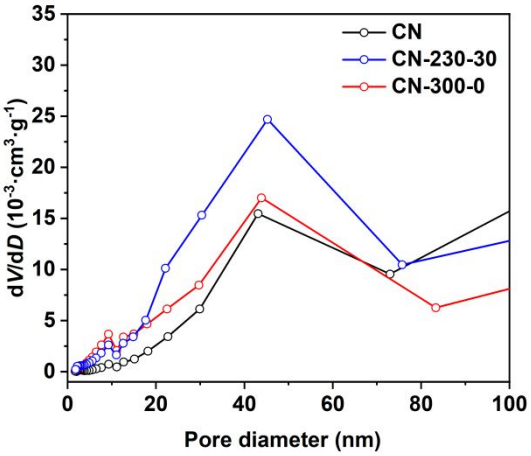

Figure S16. BJH pore size distribution from 2–100 nm based on the desorption isotherms for CN, CN-230-30 and CN-300-0.

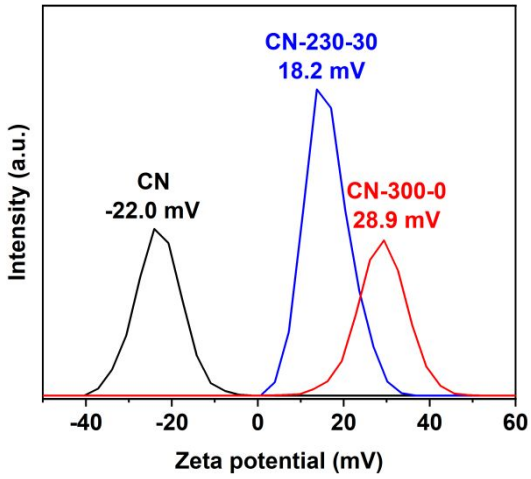

Figure S17. Zeta-potential curves for CN, CN-230-30 and CN-300-0.

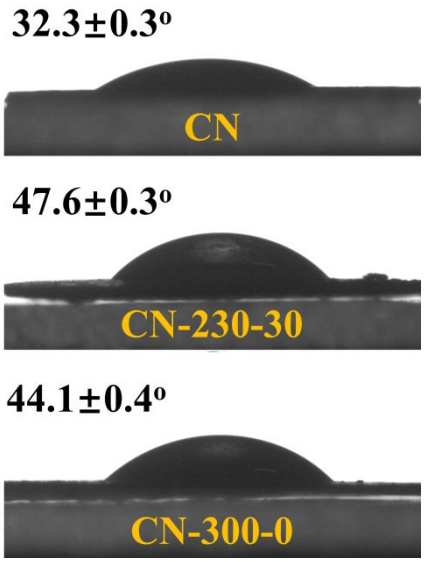

Figure S18. Photos of water contact measurement (equilibrium time of 9.0 s) for CN, CN-230-30 and CN-300-0.

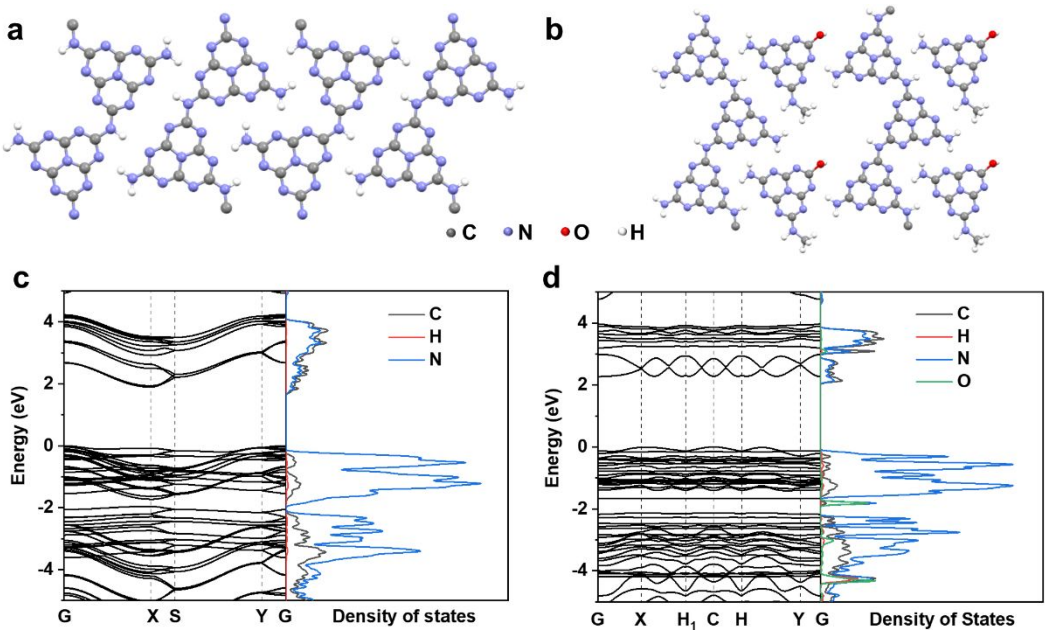

Figure S19. Structure models of (a) g-C_3N_4 and (b) Q-PHI. Calculated electronic band structures and corresponding density of states of (c) g-C_3N_4 and (d) Q-PHI. The Q-PHI model with one methyl and one hydroxyl group is selected for calculation in (b, d).

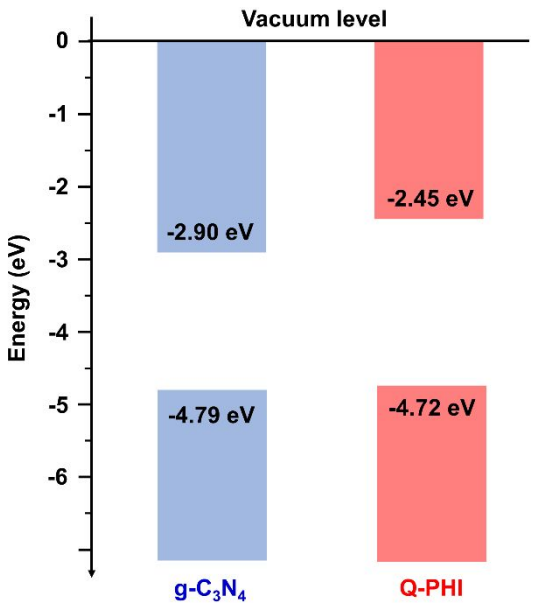

Figure S20. Electronic band structure alignments of g-C_3N_4 and Q-PHI.

Supplementary tables

Table S1. Preparation conditions and photocatalytic H_2-evolution rates of modified g-C_3N_4 by MeOH solvothermal posttreatment.

Run	Sample	Temperature (°C)	Residence time (min)	H_2-evolution rate (μmol·h^{-1})	Run	Sample	Temperature (°C)	Residence time (min)	H_2-evolution rate (μmol·h^{-1})
1	CN-230-5	230	5	9.4	22	CN-260-3	260	3	46.0
2	CN-230-10	230	10	9.2	23	CN-260-4	260	4	26.9
3	CN-230-20	230	20	17.1	24	CN-260-5	260	5	23.0
4	CN-230-30	230	30	18.0	25	CN-260-7	260	7	13.1
5	CN-230-40	230	40	11.4	26	CN-270-0	270	0	23.6
6	CN-240-3	240	3	28.7	27	CN-270-1	270	1	47.4
7	CN-240-5	240	5	36.3	28	CN-270-2	270	2	30.8
8	CN-240-7	240	7	29.5	29	CN-270-3	270	3	13.2
9	CN-240-10	240	10	23.8	30	CN-270-5	270	5	0.0
10	CN-250-0	250	0	12.3	31	CN-280-0	280	0	42.3
11	CN-250-1	250	1	32.5	32	CN-280-1	280	1	40.9
12	CN-250-2	250	2	35.8	33	CN-280-2	280	2	5.7
13	CN-250-3	250	3	24.7	34	CN-280-3	280	3	0.0
14	CN-250-4	250	4	35.8	35	CN-290-0	290	0	37.2
15	CN-250-5	250	5	38.8	36	CN-290-1	290	1	36.8
16	CN-250-6	250	6	34.7	37	CN-290-2	290	2	0.1
17	CN-250-7	250	7	37.3	38	CN-300-0	300	0	50.1
18	CN-250-10	250	10	14.9	39	CN-300-1	300	1	17.1
19	CN-260-0	260	0	8.7	40	CN-320-0	320	0	27.9
20	CN-260-1	260	1	38.9	41	CN-340-0	340	0	0.0
21	CN-260-2	260	2	42.4					

Table S2. Comparison of represented solvothermal posttreatment strategies for g-C_3N_4 modification towards photocatalytic H_2 evolution.

Photocatalyst	Amount of g-C_3N_4 and chemical	Solvothermal condition	Multiple[a]	Reference
g-C_3N_4/Q-PHI isotype composite	500 mg g-C_3N_4, 5 mL methanol	300°C, 0 min	7.2	This work
Amino-modified g-C_3N_4	50 mg g-C_3N_4, 30 mL ethylene glycol, 20 mg urea	160°C, 6 h	5.5	[1]
Fluorine modified g-C_3N_4 nanosheets	250 mg g-C_3N_4 nanosheets, 500 g HF (>40%), 30 mL ethanol	140°C, 6 h	1.3	[2]
g-C_3N_4 modified by sugar	400 mg bulk g-C_3N_4, 40 mg fructose, 60 mL water/ethanol (v:v = 1:1)	180°C, 6 h	13	[3]
Monolayer g-C_3N_4 nanomesh	100 mg porous g-C_3N_4, 300 mL water/isopropanol (v:v = 2:3)	120°C, 24 h	5.5	[4]
Holey defect g-C_3N_4	1000 mg g-C_3N_4, 70 mL methyl alcohol	200°C, 6 h	4.9	[5]
	1000 mg g-C_3N_4, 70 mL isopropyl alcohol	200°C, 6 h	7.4	
	1000 mg g-C_3N_4, 70 mL tetrahydrofuran	200°C, 6 h	13.9	
	1000 mg g-C_3N_4, 70 mL *N*,*N*-dimethylformamide	200°C, 6 h	5.6	
Fish-scale structured g-C_3N_4 nanosheet	200 mg g-C_3N_4 nanosheet, 30 mL ethylene glycol, a certain amount of PVP/CTAB	80°C, 12 h	2.9	[6]
(Na, O)-g-C_3N_4	500 mg bulk g-C_3N_4, 500 mg NaOH, 60 mL ethanol	160°C, 10 h	6.9	[7]

a] $\text{Multiple} = \frac{\text{Photocatalytic H2 — evolution activity of modified g — C3N4}}{\text{Photocatalytic H2 — evolution activity of original g — C3N4}}$

Table S3. Q-PHI models with different grafted groups and corresponding chemical formulas of exfoliated units.

Q-PHI model	Grafted group	Chemical formula of exfoliated unit
Two methyl groups	$(–CH_3)_2$	$(C_6N_7)(NH_2)(OH)_2$
One methyl group and one hydroxyl group	$–CH_3$, –OH	$(C_6N_7)(NH_2)(OH)(NH)(CH_3)$
Two hydroxyl groups	$(–OH)_2$	$(C_6N_7)NH_2(NH)_2(CH_3)_2$

Table S4. C 1s, N 1s and O 1s peak-area percentages (%) of different C species, N species and O species for CN, CN-230-30 and CN-300-0.

Sample	C 1s				N 1s				O 1s			
	C–C	C–N	N=C–N	C–OH	C–N=C	$N–(C)_3$	N–H	N–C–OH	π charging	Adsorbed –OH	Doped O	C–OH
CN	64.7	25.0	10.2	0	37.5	31.5	23.6	0	7.4	47.6	52.4	0
CN-230-30	42.0	18.8	35.8	3.4	30.3	22.0	35.5	0	14.3	38.2	61.8	0
CN-300-0	27.3	21.0	31.1	20.6	26.0	23.0	21.6	28.4	1.1	30.6	60.7	8.8

References

(1) Yang, H.; Zhang, A.; Ding, J.; Hu, R.; Gong, Y.; Li, X.; Chen, L.; Chen, P.;Tian, X. Amino Modulation on the Surface of Graphitic Carbon Nitride for Enhanced Photocatalytic Hydrogen Production. *Carbon* **2024,** *219*, 118841.

(2) Lin, W.; Lu, K.; Zhou, S.; Wang, J.; Mu, F.; Wang, Y.; Wu, Y.;Kong, Y. Defects Remodeling of g-C_3N_4 Nanosheets by Fluorine-Containing Solvothermal Treatment to Enhance Their Photocatalytic Activities. *Appl. Surf. Sci.* **2019,** *474*, 194–202.

(3) Baranowska, D.; Zielinkiewicz, K.; Mijowska, E.;Zielinska, B. Sugars Induced Exfoliation of Porous Graphitic Carbon Nitride for Efficient Hydrogen Evolution in Photocatalytic Water-Splitting Reaction. *Sci. Rep.* **2024,** *14* (1), 1998.

(4) Han, Q.; Wang, B.; Gao, J.; Cheng, Z.; Zhao, Y.; Zhang, Z.;Qu, L. Atomically Thin Mesoporous Nanomesh of Graphitic C_3N_4 for High-Efficiency Photocatalytic Hydrogen Evolution. *ACS Nano* **2016,** *10* (2), 2745–2751.

(5) Dang, T. T.; Nguyen, T. K. A.; Bhamu, K. C.; Mahvelati-Shamsabadi, T.; Van, V. K. H.; Shin, E. W.; Chung, K.-H.; Hur, S. H.; Choi, W. M.; Kang, S. G.;Chung, J. S. Engineering Holey Defects on 2D Graphitic Carbon Nitride Nanosheets by Solvolysis in Organic Solvents. *ACS Catal.* **2022,** *12* (21), 13763–13780.

(6) Lin, B.; An, H.; Yan, X.; Zhang, T.; Wei, J.;Yang, G. Fish-Scale Structured g-C_3N_4 Nanosheet with Unusual Spatial Electron Transfer Property for High-Efficiency Photocatalytic Hydrogen Evolution. *Appl. Catal. B* **2017,** *210*, 173–183.

(7) Fang, W.; Liu, J.; Yu, L.; Jiang, Z.;Shangguan, W. Novel (Na, O) Co-Doped g-C_3N_4 with Simultaneously Enhanced Absorption and Narrowed Bandgap for Highly Efficient Hydrogen Evolution. *Appl. Catal. B* **2017,** *209*, 631–636.